Prototype Development and Feasibility Assessment of a Vertically Mounted Floating Element Skin Friction Balance

Muhammad Raza

Thesis submitted to the Faculty of the
Virginia Polytechnic Institute and State University
in partial fulfillment of the requirements for the degree of

Master of Science
in
Aerospace Engineering

Kevin T. Lowe, Co-chair
William J. Devenport, Co-chair
Aurelien Borgoltz

December 19^{th}, 2024
Blacksburg, Virginia

Keywords: Wall Shear Measurement, Skin Friction Measurements, Floating Element Balance, Subsonic Wind Tunnel, Direct Method of Measurement

Copyright 2025, Muhammad Raza

Prototype Development and Feasibility Assessment of a Vertically Mounted Floating Element Skin Friction Balance

Muhammad Raza

(ABSTRACT)

Wall shear stress is one of the most essential scaling parameters used in fluid dynamics. It is significant because it helps us compare results in different experimental studies. The accurate measurements of wall shear stress will be instrumental in improving the existing empirical models and validating CFD models. Wall shear stress is also vital in improving fuel efficiency, heat transfer efficiency, and aerodynamic efficiency in real-world applications. This work discusses the design and implementation of a prototype floating element balance — a direct method of wall shear measurement. The direct measurement methods are robust and can significantly improve the validity of experimentation when perfected. In this work, a prototype floating element balance is designed and developed to estimate the wall shear stress in a smooth wall pilot facility to assess its feasibility for large-scale development. The floating element balance utilizes a strain gauge to estimate the wall shear stress. The preliminary tests show promising results, revealing potential design improvements. A strain measurement study is conducted to investigate the force-strain relationship and the reliability of the balance, which highlights the long-term stability and consistency in the strain measurement. However, further investigations are required into the drift response of the floating element balance. The strain measurements are also employed to calibrate the balance using a linear curve fit with a coefficient of determination of $R^2 = 0.99$, indicating a satisfactory linear estimation.

Prototype Development and Feasibility Assessment of a Vertically Mounted Floating Element Skin Friction Balance

Muhammad Raza

(GENERAL AUDIENCE ABSTRACT)

Drag is a phenomenon that occurs when the surface of a solid body interacts with a fluid. In fluid mechanics, there are two fundamental types of drag forces: pressure and skin friction. Pressure drag occurs due to the shape of the body, creating a pressure difference across the body, while skin friction drag arises due to the dominant viscous nature of the fluid. Understanding these forces is vital in improving the aerodynamic efficiency of various devices. Also, these forces play an essential role in the fuel efficiency and performance of the vehicles. The measurement of pressure drag is relatively straightforward compared to the skin friction drag. However, the measurement of skin friction drag can pose a challenge due to its smaller magnitude than the pressure drag. The importance of skin friction is due to its physical properties, which allow us to compare different experimental results and understand details about the turbulence in the flow. Also, accurate information on skin friction would improve existing relationships in fluid mechanics, and this information is also utilized to validate mathematical models in fluid mechanics. This work presents the design and implementation of a prototype used to estimate skin friction in a smooth wall facility using a novel and robust measurement known as floating element skin friction balance. Preliminary tests are conducted to assess the viability of the floating element balance for a large-scale development, which shows promising results while underlining some inherent limitations in the design and performance.

Acknowledgments

The past two years were some of the most challenging and exciting years I have ever faced. There were ups and downs, but it was all worth it. I have gained valuable experience, and it wouldn't have been possible without the help of many people in my life.

First, I would like to express my deepest gratitude to Dr. Todd Lowe, who was very considerate and helpful as an advisor. His course helped me so much that it became my favorite at Virginia Tech. I was able to finish this only because of his guidance. I will forever be indebted to his support and his time. I will miss working with him. Second, I would like to express my sincerest gratitude to Dr. William Devenport, who, as an advisor, gave me constructive feedback and ideas to tackle the design problems I faced. I was privileged enough to be selected to assist the SFN team with their experiments, which gave me valuable experience and helped me finish this. Experimental work can be challenging, and sometimes, we get lost in the things we can't control. His advice about "don't lose sight of the objective" is something I will never forget and carry with me. Third, I am immensely grateful to Dr. Aurelien Borgoltz for his time, guidance, and assistance while I was conducting the experiments. His door was always open for me whenever I needed to have a quick chat with him.

I would like to formally thank Sherry Gong for her support in the procurement process.

I would like to thank AOE Machine shop members, especially Scott Patrick, Cameron Hollandsworth, Roy Handy, and James Lambert, for their time and efforts in the machining process. I would like to thank John Burleson for his support in electronics and for helping me move stuff.

Of course, no academic journey is without friends, colleagues, and mentors. I would like to thank Humza Butt, a friend and mentor who always motivated me, let me ramble ideas, and gave me good advice. I would like to thank Shishir Damani for his time and help during the experiments. I would like to thank Shreyas Chaware for his time and for sharing his data with me. I would like to thank Kirubaharan Natarajan for sharing the CAD of the tunnel and spending time with me at APPL. I would like to thank the people from the AOE community, especially Bhavika Sharma, Eric Totten, Monica Shanmugam, Will Jordan, Dani Binu, Sarthak Deshmukh and Kevin Fernandez.

Special thanks to my new advisor, Dr. W. Nathan Alexander, who is very kind, understanding, and invested in my success. I am excited to work with you. I would like to thank the people from the Acoustic Chamber Charlie Galluscio, Ryan Lundquist, T-Dog, and Steve Huang.

I want to thank my family members who provided unwavering love and kind support: Mama, Baba, Brother, Uncle, Aunt, and cousins.

M Raza,
Blacksburg, VA

Contents

List of Figures ix

List of Tables xiv

1 Introduction 1

1.1 Motivation 1

1.2 Background Information 3

1.2.1 Wall Shear Stress 4

1.2.2 Turbulent Flows 5

1.2.3 Turbulent Boundary Layer 6

1.2.4 Sub-layers of Turbulent Boundary Layer 10

1.3 Brief Overview of Various Methods of Estimating Skin Friction 12

1.3.1 Indirect Methods 13

1.3.2 Direct Methods 21

1.4 Literature Review of Floating Element Balance 24

1.4.1 Brief History 24

1.4.2 Recent Developments of Floating Element Balance 25

1.4.3 Inherent Errors Associated with the Measurement 29

1.5 Scope of Research 34

2 Design Configuration **37**

2.1 Mechanical Configuration 37

2.2 Mechanical Analysis 41

2.3 Strain Measurements 44

2.4 Geometric Inconsistencies 49

3 Experimental Facility and Instrumentation **50**

3.1 Open Jet Subsonic Wind Tunnel at Virginia Tech 50

3.2 Experimental Setup 51

3.3 Data Acquisition System 52

3.4 Static Response of the Floating Element Balance 55

3.5 Uncertainty 56

4 Experimental Method and Measurements **58**

4.1 Calibration Procedure 58

4.2 Pitot Static Measurements 63

4.3 Steady Flow Measurements 65

4.4 Signal Post-processing 68

5 Conclusion **70**

5.1 Summary 70

5.2 Recommendations 71

Bibliography **73**

List of Figures

1.1 The development of the boundary layer for flow over a flat plate, different flow regimes, and the sublayers of the boundary layer[11] 7

1.2 The Sub-Layers of the Boundary Layer description by Vishwanathan [57], where U_1^+ and x_2^+ are non-dimensional streamwise velocity and wall-normal height respectively. 11

1.3 Depiction of hot-film in [56]. δ_t is the thermal boundary layer. 16

1.4 Preston tube as depicted in [56]. d and d_i are the outer and inner diameters of the Preston tube, respectively. 17

1.5 Stanton Tube as depicted in [56]. H and h are the outer and inner height of the Stanton Tube, respectively. 18

1.6 Sublayer Fence as depicted in [56] 20

1.7 The Boundary Layer Rake measurements on Spalding Fit by Butt et al. [9], where u^+ and y^+ are non-dimensional streamwise velocity and wall-normal height respectively. 21

1.8 Floating Element Balance as described in Rathakrishnan [48] 24

1.9 Schematics of the Floating Element Balance from Ferreira et al. [23] 27

1.10 Assembly of the Floating Element Balance from Baars et al. [3] 28

1.11 Misalignment caused by the tilt in the air-bearings from Baars et al. [3] . . . 29

1.12 Principle of Floating element balance from [8]. Where Z is the wall-normal height, u is the streamwise velocity, χ is the distance from the pivot center of the element to the fixed surface, d is the diameter of the element, ϵ is the element edge height, and g is the gap width. 31

1.13 Empirical relationship for floating element balance from Allen 32

1.14 Misalignment of floating element balance from Allen 33

2.1 Section View A1: Floating element balance assembly with the $3D$ printed prototype (blue: Enclosure for the balance). Detail View A2: $h_{gap} = 1.8mm$ and $h_{lip} = 2.1mm$ 39

2.2 Components of the floating element balance: (A): mounting frames, (B): flexure (position of the strain gauge), (C): counterbalancing plate, (D): floating frame, (E): flexure mounting brace, (F): floating element (shown from the non-flow side), and (G): aluminum panel rigidly fixed (enclosure hidden in the assembly) 40

2.3 Modeling of the compliant flexures as beam fixed on both ends with central point loading caused by the wall shear force 42

2.4 Diagram of displaced floating element due to the flow and deflection in the compliant mechanism (flexures), red dot represents the location of strain gauge $\approx L_{cm}$ - (Front View) 42

2.5 Diagram of displaced floating element due to the flow and deflection in the compliant mechanism (flexures), red dot represents the location of strain gauge $\approx L_{cm}$ - (Top View) 43

2.6 Diagram of the full bridge strain gauge V_{exc} is the excitation voltage and V_{out} is the signal output 45

2.7 Floating element balance mounted on extruded aluminum for the study of strain behavior in the flexure. 46

2.8 Voltage readout from the balance, where N_i is the data series and i represents the number of series. – – $\frac{|\overline{V_{out}}|}{V_{exc}}$: mean of the N_i series. 47

2.9 — ε_{cm}: calculated strain from Equation 2.6. — μ_ε: mean of the N_i series and error bars show the measurement uncertainty in the mean represented by $\pm\delta(\epsilon)$ 47

2.10 Fixed aluminum panel for the floating element balance 49

3.1 Subsonic Open Jet Wind Tunnel with modular closed test section 51

3.2 Modular Test Sections of Open Jet Wind Tunnel: open(Left) and closed(right) 52

3.3 CAD of Subsonic Open Jet Wind Tunnel with closed test section (not to scale) 53

3.4 Side schematic view of the closed test section (not to scale) 54

3.5 HGL Dynamics Hummingbird DAQ 54

3.6 Drift in the static response of the force transducer using noise rejection mode. (—) has almost 10% relative drift, indicating an unstable drift, while (—) and (—) have under 2%. 56

4.1 Floating element balance mounted on the wind tunnel wall for calibration process. 60

4.2 Calibration Data points, where N_i represents the calibration series, i represents number of series ($i = 1$ *to* 4 acquired before the wall shear measurements and $i = 5$ *to* 7 after the measurements). (– –) $\frac{|\overline{V_{out}}|}{V_{exc}}$: mean of the N_i series. 61

4.3 (—) : represents the linear fit $y = 976.44x + 5.33$ with $R^2 = 0.99$. (|o|) $\mu_{v_{out}/v_{exc}}$: mean of the N_i series and $\pm\delta(V_{out}/V_{exc})$ represents the measurement uncertainty in the mean 61

4.4 (—) : represents the linear fit $y = 976.44x + 5.33$, where y is the Force in units mN and x are the voltage output in mV/V. (o): taken before the wall shear measurements and (o): taken after the wall shear measurements 62

4.5 (—) : represents the strain measurements from Figure 2.9. (o): Calibration series before the wall shear measurements, (o): Calibration series after the wall shear measurements, and (-x -): Mean of the in situ calibration data. . . 63

4.6 (—) : represents the normalized streamwise velocity ($U_\infty \approx 20.2m/s$) courtesy of Chaware. The error bars represents the uncertainty in the streamwise velocity. 64

4.7 (– · –): represents the Spalding profile. (o): represents the velocity profile fitted to the Spalding profile. 64

4.8 Results of wall shear estimated using the mean of the $F_w(t)$. (—) : Wall shear measurement series 1, and (—) : Wall shear measurement series 2. The error bars denotes the uncertainty in the freestream velocity 66

4.9 Coefficient of Skin Friction estimated using wall shear measurements and the dynamic pressure, error bars represents the uncertainty in the freestream dynamic pressure. o: represents the result of skin friction coefficient from Spalding profile (Figure 4.7). 67

4.10 The time series of the $F_w(t)$ at $U_\infty \approx 15.30 m/s$ (—) : represents the raw time series of the signal. (—): represents the filtered signal at cutoff frequency of $\approx 2Hz$ 69

4.11 Auto spectra $G_{F_w F_w}(f)$ of the voltage response of the measurements highlights the dominant peak at $f_n \approx 2.9Hz$ 69

List of Tables

3.1 Primary uncertainties in the measurement 57

4.1 Steady flow conditions for wall shear measurements 66

Chapter 1

Introduction

1.1 Motivation

The interaction between the surface of a body and the fluid generates the drag forces. It is one of the main contributing factors in energy consumption and efficiency of aircraft, automobiles, ships, and renewable energy devices. Effects of drag are present in our daily lives, such as an aircraft traveling in the air or a truck driving on a highway. Reduction of drag in such applications would increase the fuel efficiency. Drag is generally characterized by two types: Pressure Drag, and Skin-friction Drag. In the context of a blunt body (such as a truck), the drag is primarily dominated by the pressure drag, whereas, for a streamlined body (such as an aircraft during flight), the drag is dominated by the viscous or skin-friction drag [31]. The skin-friction drag per unit area is called wall shear stress. The investigation of skin friction drag has been a popular topic in the scientific community since the early 1900s [4, 24, 51, 60, 62]. Many experimental techniques have been developed to study and quantify it [8, 63]. These techniques may involve some challenges and limitations. Although these experiments might be conducted in a more controlled environment, such as a wind

tunnel, disregarding some real-world complexities, gaining information without complexities is still essential.

Accurately measuring wall shear stress is quite significant due to its application in scaling structures in turbulent boundary layers[33]. Scaling turbulent structures is crucial for several reasons, including studying energy dissipation in turbulent boundary layers[29], which can help predict flow behavior, simplify complex flow fields, and implement optimal designs on various aerodynamic devices to reduce drag. Understanding heat transfer between the fluid and the surface, which can lead to improvements in designing heat exchangers and cooling systems, and predicting flow separation in complex geometries are also vital applications. One of the benefits of measuring wall shear stress is the ability to compare results between real-world applications and experimental data on a scaled basis.

While there are many measurement techniques that exist to estimate the wall shear stress (discussed in section 1.3), they can be challenging in implementation, repeatability, and experimental logistics. However, recent studies such as Baars et al. [3], Ferreira et al. [23] show the potential benefits of using a floating element balance for skin friction measurements (described in section 1.3.2). The primary motivation behind the design of this prototype balance is to acquire direct measurement of skin friction in the Stability Wind Tunnel at Virginia Tech **(VT SWT)** for smooth and rough walls. Recent studies at the Stability Wind Tunnel, such as Fritsch et al. [26], Vishwanathan et al. [58, 59], have used the Clauser estimation method on boundary layer rake measurements, an indirect method of approximating skin friction. Clauser estimation is discussed in section 1.3.1.

Since the magnitude of skin friction drag is approximately 20 to 60 mN depending upon the freestream velocities 16 m/s to 26 m/s, some of these challenges are associated with the design of the floating element balance sensitivity, resolution of the force transducer, and fabrication of the components of the floating element balance. The design was inspired by

the recent study of Ferreira et al. [23], where they implemented the floating element balance in a wind tunnel's floor for measuring skin friction. They conducted experiments in a low-speed wind tunnel with freestream velocity ranging from $10m/s$ to $26m/s$, increasing $2m/s$ after each measurement. Their experimental results of the floating element balance show an agreement with a hot-wire anemometry measurements. Using similar design features, such as parallel-linkage setup, floating surface area, and strain gauge transducers, and incorporating it into a different configuration, specifically a side wall of a wind tunnel, this study was conducted to gain a foundational understanding of the challenges and complexities inherent with the floating element balance as well as understanding the viability of developing a floating element balance. In addition, the floating element balance is a direct method of measurement that could significantly enhance the experimental capability and versatility for capturing the wall shear stress through direct measurements. Devising this measurement technique will open exciting new possibilities for experimenting and validating other methods.

1.2 Background Information

Before understanding the design and implementation of a floating element balance, it is essential to discuss the fundamental concepts of physics, which explain the interaction of the floating element balance and the fluid in experiments. The primary motivation in designing floating element balance is estimating the wall shear stress. The floating element balance is a direct measurement technique; there is no assumption about the flow. However, a comparison with pitot static measurements has been presented in this paper, which is an indirect measurement of wall shear stress. It is essential to compare the skin friction acquired using the floating element balance with another method of measurement. There are many

suitable methods which can be used to compare the results. Since the data was available with the closest configuration, it is sensible to use that to compare the results. The following section will discuss the difference between the two methods of measurement. This subsection will discuss wall shear stress, turbulent flows, boundary layer, and its sublayers.

1.2.1 Wall Shear Stress

The motivation section briefly describes wall shear stress. It serves as an essential scaling and comparison parameter for experimental results with different scales and conditions. Wall shear stress is defined as the streamwise momentum of a boundary layer flow along the surface that converts into a force F_w (viscous drag) acting parallel to an area S (1.1). Various studies have been conducted to study wall shear stress [46, 49]. The instantaneous wall shear stress τ_w can also be expressed as its time-averaged mean $\overline{\tau_w}$ and a zero-mean fluctuating component τ'_w, $\tau_w = \overline{\tau_w} + \tau'_w$.

$$\tau_w = \frac{F_w}{S} \tag{1.1}$$

Alternatively, the wall shear stress is also expressed as the coefficient of skin-friction, where the wall shear stress is normalized by the dynamic pressure q of the flow defined as Equation 1.2, ρ is the density of the fluid and U_∞ is the freestream velocity of the flow.

$$q = \frac{1}{2}\rho U_\infty^2 \tag{1.2}$$

$$C_f = \frac{\tau_w}{\frac{1}{2}\rho U_\infty^2} \tag{1.3}$$

Wall shear stress is also required to determine the shear or frictional velocity near the wall. The frictional velocity indicates the influence of wall shear stress in the boundary layer. The frictional velocity u_τ is used to characterize the turbulent flow structures in wall-bounded flows. It quantifies streamwise momentum due to the turbulent structures close to the wall and the shear between the layers in the flow. It represents how the wall shear stress is related to the streamwise velocity.

$$u_\tau = \sqrt{\frac{\tau_w}{\rho}} \tag{1.4}$$

In addition, the frictional velocity is used to define the non-dimensional velocity u^+ Equation 1.5, and the non-dimensional wall-normal height y^+ Equation 1.6, where y is the wall-normal height, and ν is the kinematic viscosity of the fluid. These wall parameters will be discussed in the following subsection.

$$u^+ = \frac{u}{u_\tau} \tag{1.5}$$

$$y^+ = \frac{y u_\tau}{\nu} \tag{1.6}$$

1.2.2 Turbulent Flows

Turbulence is a comprehensive topic, but it is vital in understanding the wall shear stress in turbulent flows. In this work, we will briefly discuss turbulence and its relevance to wall shear stress. Turbulence is characterized as a chaotic state of the fluid. The highly irregular velocity fluctuations and mixing of the fluid is known as turbulence. This mixing of fluid is carried out by the transfer of momentum and energy by the turbulent structures or eddies.

These eddies are formed to maintain the energy transfer between large and small structures. This transfer of kinetic energy is called energy cascades in turbulent flows.

In contrast, laminar flow is where the fluid flow is smooth and ordered. All kinds of fluid flows start as a laminar flow and transition into a turbulent flow. Turbulence can be caused by several factors, such as the characteristic length over which the fluid is flowing, increase in velocity, disturbance of the flow due to geometry, and pressure gradients present in the flow. Such external factors may contribute to a turbulent flow. It is important to note each of these factors when conducting experiments in a wind tunnel. Turbulence is a property of the flow which is mathematically represented by the Reynolds Number.

$$Re = \frac{\rho U L}{\mu} \tag{1.7}$$

Where ρ is the density of the fluid, U is the velocity of the fluid, L is the characteristic length of the surface or a body, and μ is the dynamic viscosity of the fluid. The Figure 1.1 shows a wall-bounded flow over a flat plate in which no boundary layer is formed at the leading edge ($L = 0$). The fluid flows over the length of the flat plate until reaching the characteristic length of $L = x_{cr}$, which is the critical length at which Reynolds number is approximately $Re > 5 \times 10^5$. This inequality is where the transition region starts, where the laminar flow transitions into a turbulent flow. Understanding this critical characteristic length is crucial because it signifies whether the flow is laminar or turbulent.

1.2.3 Turbulent Boundary Layer

The boundary layer is formed when a surface and a fluid interact. It is a thin region between the fluid and the surface. In this region, the fluid in contact with the solid surface of a body

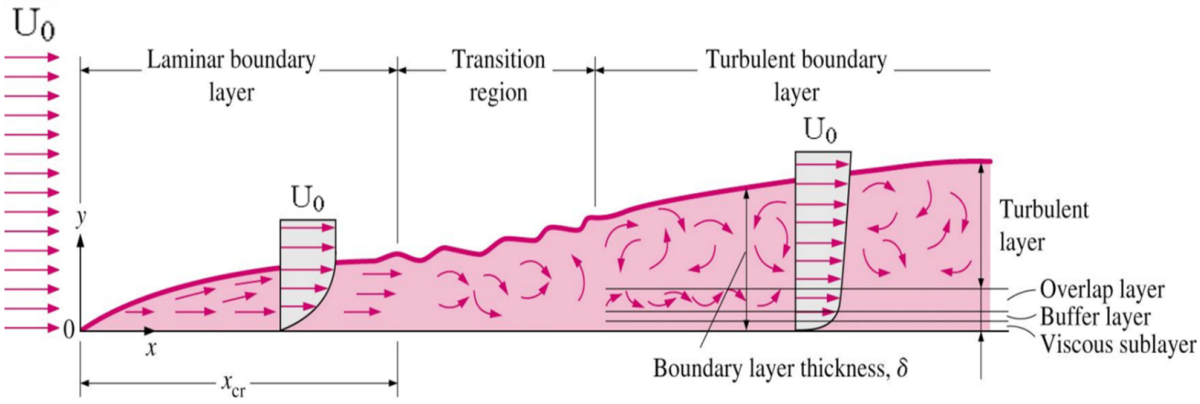


Figure 1.1: The development of the boundary layer for flow over a flat plate, different flow regimes, and the sublayers of the boundary layer[11]

.

is at rest; this is called a no-slip condition. This thin layer of fluid is dominated by the effects of viscosity, where the fluid layers closest to the surface will resist the flow the most. Within the boundary layer, the velocity from the solid surface, which is zero, gradually increases until it reaches the edge of the boundary layer, almost equal to the velocity in the freestream region. This edge velocity U_e is typically 0.99 of freestream velocity U_∞. In different applications, the edge velocity U_e or freestream velocity U_∞ is used to normalize the boundary layer profile. The boundary layer thickness δ is defined as the wall-normal height from the no-slip condition to the edge velocity. If the pressure gradients are present in the flow, that will affect the boundary layer thickness. A favorable pressure gradient will decrease the boundary layer thickness, while an adverse pressure gradient will increase the boundary layer thickness. Understanding the boundary layer is crucial because it allows us to express wall shear stress τ_w in terms of the velocity gradient near the wall (at $y = 0$) and the dynamic viscosity of the fluid μ. The Equation 1.8 signifies the wall shear stress that arises due to the interaction of the fluid and solid surface. The boundary layer region has dominant viscous effects, leading to the velocity gradient within the boundary layer. This velocity gradient causes the wall shear stress in the flow, which indicates a directly

proportional relationship with the wall shear stress.

$$\tau_w = \mu \frac{\partial u}{\partial y}\bigg|_{y=0} \tag{1.8}$$

In terms of wall-bounded flows for a flat plate, there are exact solutions for steady laminar boundary layer flows in zero pressure gradient, such as the Blasius boundary layer method [7], which is helpful in gaining velocity profile, wall shear stress, and boundary layer thickness. However, there are no exact solutions for turbulent boundary layers. The flow becomes complex at a high Reynolds number due to velocity and pressure fluctuations in the boundary layer, resulting in a turbulent boundary layer. There are empirical methods for characterizing the turbulent boundary layer, such as the von Kármán momentum integral equation, which is suitable for both laminar and turbulent boundary layers. The von Kármán integral method is useful in estimating the boundary layer thickness δ, displacement thickness δ^*, momentum thickness θ, and wall shear stress. However, it does not provide the velocity profile within the boundary layer [55]. Another empirical method for turbulent boundary layers is the power law, which is suitable for a range of Reynolds number $5 \times 10^5 < Re < 10^7$ [18]. It is a simplified empirical approximation across the boundary layer [50]. The power law utilizes an empirical relationship to define the velocity profile in the turbulent boundary layer over a flat plate. Even though it's a simple approximation of how the velocity profile changes with the wall-normal distance in wall-bounded flows, it is quite useful to get a rough estimate of the boundary layer velocity profile.

Alternatively, the turbulent boundary layer can be modeled using numerical simulations such as DNS (Direct Numerical Simulations)[38, 40], RANS (Reynolds Averaged Navier-Stokes)[39], and LES (Large Eddy Simulation)[54] models. However, these methods are computationally expensive at high Reynolds numbers, as they need finer mesh resolution to

resolve the smallest flow details. Moreover, all the numerical methods involve a certain level of approximation, making them less feasible than the empirical methods.

The Reynolds number determines the state of the boundary layer. At a high Reynolds number, the boundary layer will be considered turbulent. There are other key parameters that characterize the influences of the boundary layer with the flow, such as displacement thickness δ^*, momentum thickness θ, and the boundary layer shape factor H.

The boundary layer displacement thickness is an artificial displacement from the zero velocity point for an inviscid boundary layer required to have the same mass flow deficit as the viscous boundary layer. For an incompressible fluid flow, this is represented by the velocity deficit as $U_e - u(y)$, where $u(y)$ represents the streamwise velocity at y and y is the wall-normal distance. Due to the viscous effects, the boundary layer has an effective displacement, which acts as an increase in the solid surface boundary, thus reducing the mass flow rate.

$$\delta^* = \int_0^\delta \left(1 - \frac{u(y)}{U_e}\right) dy \tag{1.9}$$

The boundary layer momentum thickness is similar to the displacement thickness. It is defined as the displacement required from the zero velocity point for an inviscid boundary layer to have the same momentum loss as a viscous boundary layer. The momentum thickness essentially characterizes the thickness of the shear stress, a region of displacement where the viscous effects have become dominant.

$$\theta = \int_0^\delta \frac{u(y)}{U_e}\left(1 - \frac{u(y)}{U_e}\right) dy \tag{1.10}$$

The shape factor of the boundary layer is a ratio between displacement thickness and momentum thickness. In addition, it also provides the shape of the velocity profile of a boundary

layer. The shape factor for a turbulent boundary layer flow is around 1.5, and laminar flows have a higher shape factor. A high shape factor for a turbulent flow would mean instability, or the boundary layer is close to separation.

$$H = \frac{\delta^*}{\theta} \tag{1.11}$$

1.2.4 Sub-layers of Turbulent Boundary Layer

The turbulent boundary layer can be decomposed into two regions: an inner region and an outer region (Figure 1.1, and Figure 1.2 in wall units). This decomposition of the boundary layer is denoted by the viscous wall units as u^+ and y^+ previously mentioned in subsection 1.2.1 as Equation 1.5 and Equation 1.6. The importance of using these units lies in the difficulty of characterizing the flow with global parameters of the boundary layer, such as thickness and edge velocity. These units also allow the flow to become non-dimensionalized and introduce simplicity in comparison across different flow conditions. The wall unit's scaling also highlights the turbulence behavior in the near-wall region. The inner region consists of a viscous sublayer, which, due to dominant viscous effects, essentially acts as a laminar flow. The velocity profile of this layer is nearly linear, and there is no velocity fluctuations. Due to the overwhelming viscous effects, the velocity is linearly dependent upon the wall-normal distance, as described in the Equation 1.12. The viscous sublayer is from $0 < y^+ < 5$ [50].

$$u^+ = y^+ \tag{1.12}$$

After the viscous sublayer, the buffer layer exists, a transitional region where both the vis-

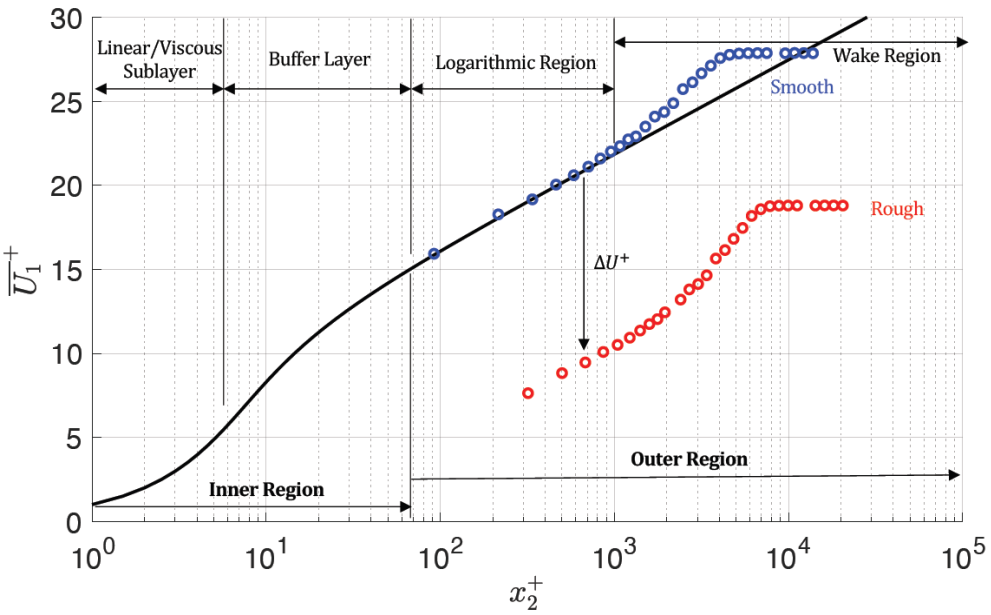


Figure 1.2: The Sub-Layers of the Boundary Layer description by Vishwanathan [57], where U_1^+ and x_2^+ are non-dimensional streamwise velocity and wall-normal height respectively.

cous and turbulent effects are significant. The buffer layer has more thickness than the viscous sublayer. The velocity profile of this layer is not linear, but it exhibits both linear and logarithmic characteristics. The buffer layer extends from $5 < y^+$ until $30 > y^+$ [50]. An overlap exists between the inner and outer regions. This overlap follows a logarithmic velocity profile. In this logarithmic layer, the flow is dominated by turbulence with velocity fluctuations, which is a key characteristic of turbulence. Although turbulence has a significant influence in this layer, the viscous effects are still present. The phenomenon of this overlap between the inner and outer regions is also known as the Logarithmic Law of the Wall and is expressed as the Equation 1.13, where κ is the von Kármán constant (approximately 0.41 for turbulent flows) and B is a constant that depends on the flow conditions (typically around 5.0, depending upon flow regime, roughness of the surface and Reynolds number). The log layer extends from $y^+ \approx 30$ to $y^+ \approx 300$ [50].

$$u^+ = \frac{1}{\kappa}\ln(y^+) + B \tag{1.13}$$

In the outermost region, the velocity profile no longer follows the logarithmic profile. Since this region is farthest from the wall, the velocity approaches near the freestream velocity. The global parameters, boundary layer thickness δ, and the edge velocity U_e are used to describe this region. In the outer region, the viscous effects are less significant, and the influence of turbulent fluctuations is dominant. The Law of the Wake governs this region, first proposed by Coles [15]. This region is also sensitive to pressure gradients, which will affect the edge velocity of the boundary layer. In the Equation 1.14, Π represent the wake profile parameter and the term $w(\frac{y}{\delta})$ represents the wake function, which describes the velocity profile in the outermost region of the turbulent boundary layer; typically, a sine function is used to model the wake contribution in the turbulent boundary layer.

$$u^+ = f\left(\frac{yu_\tau}{\nu}\right) + \frac{\Pi}{\kappa}w\left(\frac{y}{\delta}\right) \tag{1.14}$$

1.3 Brief Overview of Various Methods of Estimating Skin Friction

The need to accurately measure skin friction has been briefly discussed in the motivation and background information section, reiterating that skin friction is the resistive force that is generated due to interaction between a body's surface and a fluid flowing over it. It is caused by the viscous effects. Wall shear stress and friction velocity are important scaling parameters that are used to understand turbulent structures and energy dissipation in the boundary layer. Furthermore, it is quite useful in simplifying a complex flow field, which

can help implement various aerodynamic design optimizations. Lastly, these parameters are used to compare the results of different experimental studies.

As mentioned previously, the estimation of skin friction is generally divided into two experimental techniques: Indirect Methods and Direct Methods. This section will briefly discuss the two methods of estimating skin friction in a general format.

1.3.1 Indirect Methods

The indirect methods utilize the relationships and assumptions associated with the flow conditions. These relationships are used to infer the wall shear stress. The indirect methods require the properties of the fluid and the flow. In addition, the assumptions about the flow, boundary layer parameters, and velocity. Indirect methods include:

- Pressure gradient method
- The momentum integral method.
- Heat transfer relationship.
- Study of flow about an obstacle.
- Clauser estimation.

Pressure Gradient Method

The pressure gradient method uses the average pressure drop over the length of a duct or a channel. This method is reliable for both laminar flows and turbulent flows. However, there are a few limitations to this method. In order to get reliable results, this method requires to have a long enough length of the duct for the flow to fully develop. This would cause all

of the streamwise gradients present in the flow to become zero except for the pressure. In addition, the flow channel should be uniform without irregularities, meaning there should be no change in cross-sectional area or surface roughness. The pressure gradient across the pipe can be related to the integrated wall shear stress of the flow over the surface area of the pipe [29].

$$\overline{\Delta P} A = \int_S \overline{\tau_w}\, ds \tag{1.15}$$

Where ΔP is the pressure difference between two points in a fully developed flow, A is the cross-sectional area of the pipe or a pipe, S is the surface area along which the fluid flows. Since this method uses the average pressure drop, it can only approximate the mean wall shear stress $\overline{\tau_w}$. Simplifying Equation 1.15, we can express the mean wall shear stress $\overline{\tau_w}$ as following:

$$\overline{\tau_w} = \frac{\overline{\Delta P} A}{S} \tag{1.16}$$

von Kármán Momentum Integral Method

This method applies the momentum integral method developed by von Kármán, which is valid for both turbulent flow and laminar flows. It requires accurate information about the boundary layer parameters such as velocity profile, displacement thickness, momentum thickness, and boundary layer shape factor[8, 29]. These parameters are used to relate the mean wall shear stress by the following relation:

$$\overline{\tau_w} = \rho U_e^2 \left(\frac{d\theta}{dx} + (H+2) \frac{\theta}{U_e} \frac{dU_e}{dx} \right) \tag{1.17}$$

This method is considered the most accurate if the approximation of boundary layer parameters are accurate. These measurements are quite challenging to obtain for $3D$ wall-bounded flows. The Equation 1.17 is only applicable for the 2D wall-bounded flow measurements which is a simplified form of the momentum integral equation.

Heat Transfer Method

The heat transfer method is based on using a thin hot-film that is flush-mounted in an undisturbed flow where the local skin friction can be inferred by the heat transfer between the flow and the hot-film[29, 34]. This relationship between skin friction and heat transfer is called the Reynolds Analogy.

$$St \cdot \mathrm{Pr}^{2/3} = \frac{C_f}{2} \tag{1.18}$$

$$St = \frac{Nu}{Re \cdot \mathrm{Pr}} \tag{1.19}$$

In the Equation 1.18, St is the Stanton number, which is a non-dimensional number that represents a ratio of the convective heat transfer in the flow and the thermal properties of the fluid. Pr is the Prandtl number, which is a dimensionless number that represents the ratio of the momentum diffusivity to the thermal diffusivity in a fluid flow. Furthermore, the Stanton number can also be represented as Equation 1.19, where Nu is the Nusselt number, which is also a non-dimensional number that represents the ratio of the convective heat transfer to the conductive heat transfer between a surface and the boundary layer of the flow.

Since the hot film is flush-mounted, the region of the boundary layer in contact with the

film is the laminar sublayer[44]. The hot film is electrically heated, which maintains a constant temperature. The convective heat loss due to the fluid flow cooling the film can be obtained by measuring the power input. The convective heat loss is typically assumed to be proportional to the power fed to the hot film to maintain the temperature. The empirical relation for estimating the wall shear stress is as follows:

$$U_{hf}^2 = A + B\tau_w^n \tag{1.20}$$

U_{hf} represents the voltage of the thin hot-film, n typically ranges from 0.25 and 0.3, and A and B are the calibration constants that depend upon the flow conditions, hot-film temperature, and the mounting material for the hot-film. This method works well where the Reynolds Analogy can be applied[44].

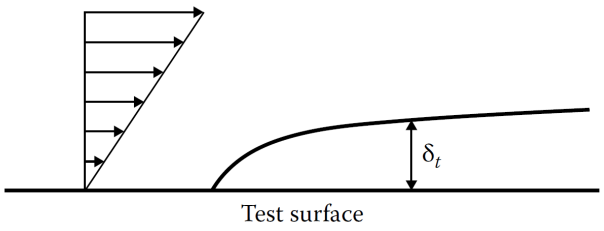


Figure 1.3: Depiction of hot-film in [56]. δ_t is the thermal boundary layer.

Flow about an Obstacle

This method uses the Preston tube, the Stanton tube, and the Sublayer fence to relate the pressure gradient about these obstacles with the wall shear stress. The obstacles must be small enough to be completely immersed in the near-wall region of the boundary layer, where the law of the wall is applicable. In addition, these obstacle should have a negligible impact on the growth of the boundary layer.

The Preston tube is most commonly used for estimating wall shear stress due to its simple setup and ease of application. The Preston tube is placed on the wall. Its diameter is usually large enough that it covers up to the log region of the velocity profile, allowing the law of the wall to be applicable. The Preston tube measures the dynamic pressure of the flow, which is proportional to the local streamwise velocity of the flow. The dynamic pressure can be related to wall shear stress obtained by an empirical curve fit using the logarithmic law of the wall[29, 44]. Therefore, the Preston tube method will fail in any flow conditions where this law is invalid, for instance, the leading edge of a flat plate, wall roughness effects, and severely adverse pressure gradients.

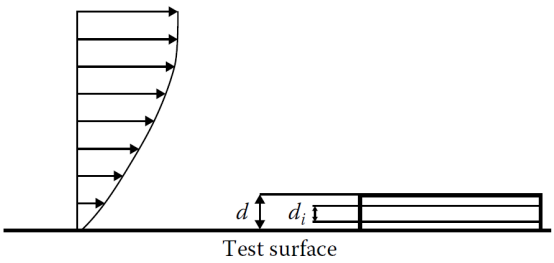


Figure 1.4: Preston tube as depicted in [56]. d and d_i are the outer and inner diameters of the Preston tube, respectively.

$$u^+ = \int_0^{y^+} \frac{2\,dy^+}{1 + \sqrt{1 + 4\kappa^2 y^+ \left[1 - \exp\left(-\frac{y^+}{A^+}\right)\right]^2}} \tag{1.21}$$

$$\tau_w^+ = \left(\frac{u_\tau d/2}{\nu}\right)^2 \tag{1.22}$$

$$q^+ = \frac{1}{2}\left(u^+ \frac{u_\tau d/2}{\nu}\right)^2 \tag{1.23}$$

In the Equation 1.21, κ is the von Kármán constant (approximately 0.41) and A^+ is an

empirically obtained constant of turbulence (typically around 26). This non-dimensional velocity can be used in to find q^+, u^+ represents the velocity in the inner region of the boundary layer.

In the Equation 1.22 and Equation 1.23, τ_w^+ is the dimensionless wall shear stress, q^+ is the dimensionless dynamic pressure, d is the diameter of the Preston tube. These parameters can be calculated from the viscous wall units of the boundary layer.

The Staton tube is very similar to the Preston tube. Typically, the Stanton tube is made of a rectangular opening Pitot tube. A simple Stanton tube can be thought of as placing a pitot-static pressure port on the wall and carefully covering it with a razor blade. The edge of the sharp razor will divert the flow only from the viscous sublayer to the pressure port[29]. The dynamic pressure measured through the Preston tube covers the whole inner region of the boundary layer.

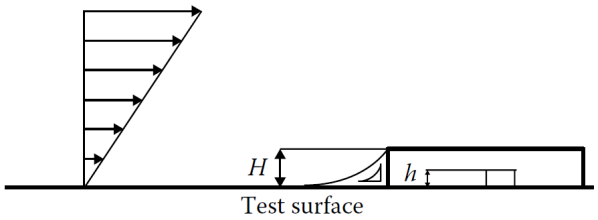


Figure 1.5: Stanton Tube as depicted in [56]. H and h are the outer and inner height of the Stanton Tube, respectively.

In contrast, the Stanton tube is only immersed in the viscous sublayer of the boundary layer. The Staton tube measures the pressure, which has contributions from both the wall shear stress and the deflection of the flow due to the presence of the Stanton tube in the flow but which of the two will dominates is dictated by the dimension H of the Statnton tube and the wall shear stress. Similar to the Preston tube, it is facing upstream towards the incoming flow. The approximated pressure is used to relate the wall shear stress of the flow

empirically. In the Equation 1.24 Re_τ is the frictional Reynolds number, $\overline{\tau_w}$ is the mean wall shear stress, and H is the height of the Staton Tube. H is the most crucial parameter, which is the overall height of the tube. The flow separates just before reaching the upstream face of the tube, and the separation streamline aligns with the edge of the upstream face. The wall shear stress causes the pressure differential on the flow-facing opening of the Stanton Tube.

$$Re_\tau = \frac{\overline{\tau_w}\rho H^2}{\mu^2} \tag{1.24}$$

The Sublayer Fence is also quite similar to the Preston Tube. It is made up of a small (metallic) strip carefully placed between two pressure ports. The height of the fence should be small enough that it is fully submerged in the viscous sublayer of the boundary layer. The pressure difference across the fence in the two ports is a function of the wall shear stress. The pressure difference between the upstream and downstream faces of the fence can be correlated by the velocity distribution in the laminar sublayer, which is linear[44]. This method also uses similar equations as Equation 1.22 and Equation 1.23. However, the equation for non-dimensional velocity is Equation 1.5 described in subsection 1.2.4. Similarly, other variations of obstacles, such as the square ridge and fixed wall hot-wire, are used similarly to relate the pressure difference with the wall shear stress.

Clauser Estimation

The Clauser estimation utilizes the boundary layer velocity profile acquired from different methods of velocity measurements, such as The Boundary Layer Rake, Hot-wire Anemometry, Laser Doppler Anemometry, and Particle Image Velocimetry. However, the latter two are experimentally complex. This estimation was proposed by Clauser [14]. The Clauser

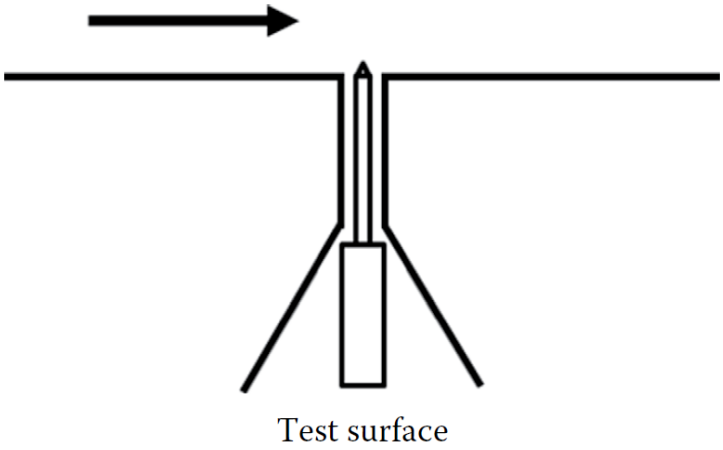


Figure 1.6: Sublayer Fence as depicted in [56]

estimation is based on the valid assumption of the Logarithmic law of the wall. An assumed value of u_τ is iteratively used until the velocity profile falls on the logarithmic segment of the velocity profile, defined as a Spalding Fit[52]:

$$y^+ = u^+ + e^{(-\kappa B)}\left\{e^{(\kappa u^+)} - 1 - \kappa u^+ - \frac{(\kappa u^+)^2}{2!} - \frac{(\kappa u^+)^3}{3!} - \frac{(\kappa u^+)^4}{4!}\right\} \tag{1.25}$$

In the Equation 1.25, κ is the von Kármán constant and B is a constant which depends on the flow conditions, typically around 5. The closest fit of u^+ would be to calculate the frictional velocity u_τ, which can be used to determine the wall shear stress. Alternatively, a relationship between the frictional velocity u_τ and coefficient of skin friction C_f is used, which is defined as:

$$\frac{u_\tau}{U_e} = \sqrt{\frac{C_f}{2}} \tag{1.26}$$

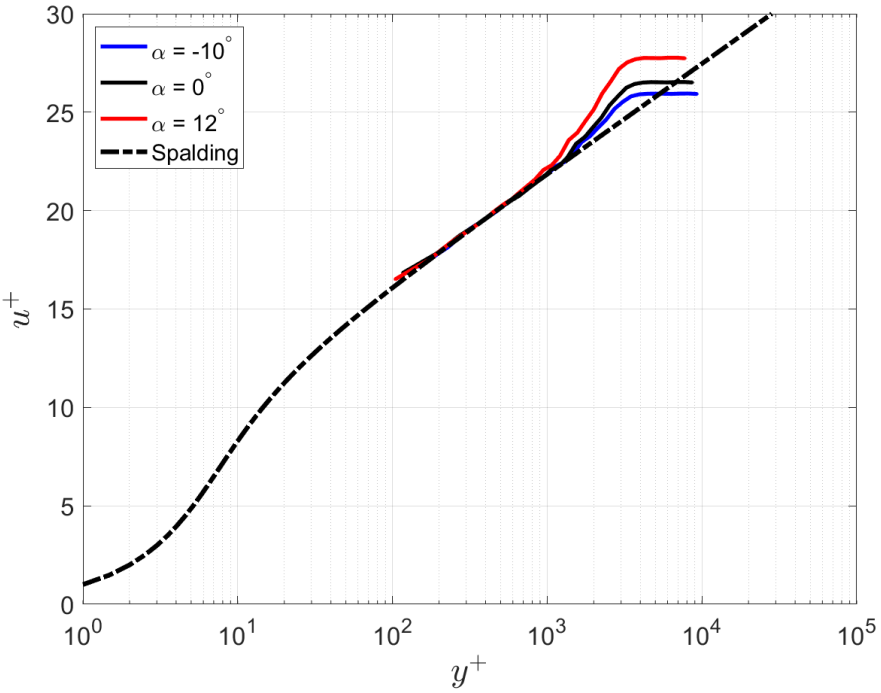


Figure 1.7: The Boundary Layer Rake measurements on Spalding Fit by Butt et al. [9], where u^+ and y^+ are non-dimensional streamwise velocity and wall-normal height respectively.

1.3.2 Direct Methods

The direct method captures the skin friction of the fluid in the flow. These methods are best for accurately measuring skin friction because they do not require any assumption of the flow or fluid properties. Direct Methods include:

- Oil Film Interferometry
- MEMS-based Wall Shear Sensor
- Floating Element Balance

Oil Film Interferometry

OFI technique uses a thin layer of oil applied on a surface in a test section of an experimental facility. The sensitive nature of the oil will allow the oil film to be displaced due to various flow conditions such as wall shear stress, pressure gradients, surface geometry, oil properties, and gravity. Although this oil film is affected by various conditions, skin friction is the most dominating force. The thinning of the oil is measured by the using interferometry[53]. This rate of thinning of oil film can be used to approximate wall shear stress due to the relation Equation 1.27.

$$\tau_w = \frac{\mu_{\text{oil}} x}{ht} \tag{1.27}$$

$$h = \frac{\lambda\phi}{4\pi}\left(\frac{1}{\sqrt{n_{oil}^2 - n_{air}^2 \sin^2\theta}}\right) \tag{1.28}$$

The Equation 1.28 describes the relationship between the interference of the oil film and the oil thickness h. As described in [43], the thickness of the oil film h can be determined using the wavelength of a light source λ (typically used as a monochromatic and coherent light source) emitted and strikes the oil at an incidence angle of θ. Part of the incident light is reflected from the oil (n_{oil},n_{air} is the refractive indices of the oil and air), and the remaining is reflected back from the surface beneath the oil. This creates an interference pattern. The interference depends on the phase difference between the two, which is captured by a high-resolution camera.

MEMS-based Wall Shear Sensor

MEMS stands for micro-electromechanical systems, which incorporate both electronic and mechanical components. Typically, in aerospace applications, these are micromachined silicon-based sensors. The dimensions of MEMS-based sensors are $120\mu m \times 120\mu m \times 7\mu m$[43]. Due to this small size, these are proven to be the most effective in the wall shear stress measurements. The MEMS-based sensors operate on the principle of capacitance. The sensor is flush-mounted in the flow, and the design allows a thin, moveable surface with an embedded conductor to be displaced by the flow. This floating surface is connected with thin tethers in a silicon housing with a passivated electrode. The floating element and the fixed surface are separated by a thin region, acting as a dielectric medium. The differential capacitance measures the wall shear stress. This can be achieved by calibrating the sensor in a laminar flow cell with varying flow velocity. Some other MEMS-based shear sensors operate on heat-based and optic-based methods to measure wall shear stress.

Floating Element Balance

The traditional floating element balance is quite similar to MEMS-based sensors. However, it uses conventional machining and fabrication. The floating surface experiences the wall shear force of a boundary layer on a small area. It can either freely displace due to the shear force acting on the surface (displacement type) or use an in-built mechanism that restores the element to its neutral position (restoring type). The most basic floating element balance would consist of a floating surface, which is flush-mounted in the flow, and a transducer, which holds the floating surface, where the transducer measures the displacement or the force due to the displacement[3, 19, 23, 48]. More details regarding the floating element balance are discussed in the next section.

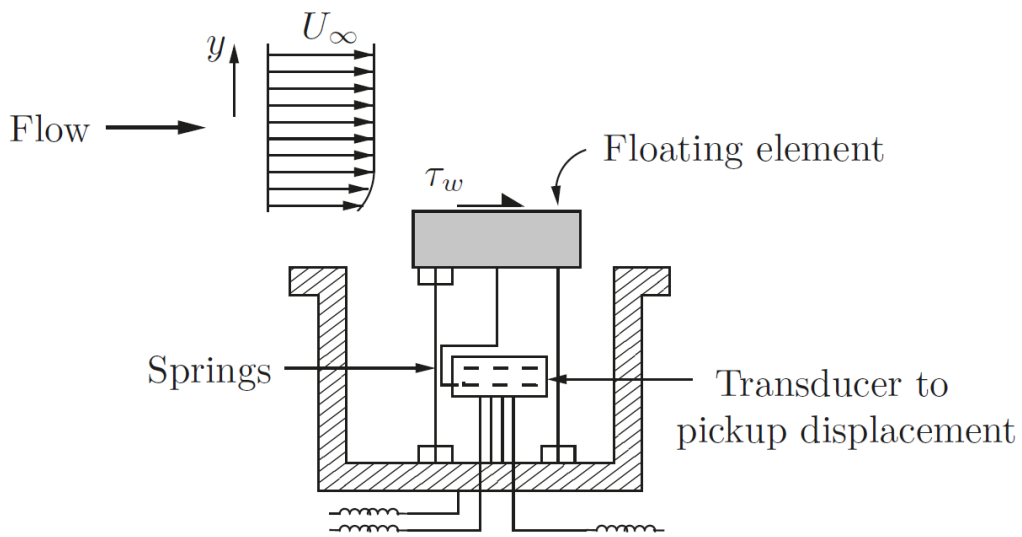


Figure 1.8: Floating Element Balance as described in Rathakrishnan [48]

1.4 Literature Review of Floating Element Balance

This section will discuss a brief history of the concept of floating element balance, the recent developments of floating element balance, and systematic sources of errors in floating element balance.

1.4.1 Brief History

A similar concept as the floating element was first designed by Froude over a hundred and fifty years ago. The design consisted of thin, flat wooden planks towed in a water tank, and a mechanical dynamometer was used to estimate the force. By varying velocities and different surface finishes for the planks, Froude measured the force experienced by the planks and plotted them as a function of velocity. Since the planks were thin and flat, the force was primarily due to the resistance or drag [6, 41]. Still, at that time, the viscous effects of the boundary layer were not understood. After Prandtl, which is foundational in

our understanding of the boundary layer and the significance of drag, years later, a similar experiment was conducted by Kempf in which the floating element balance was attached on the bottom of a pontoon boat. Notably, Dhawan is considered a pioneer in perfecting the floating element balance for direct measurement. The design consisted of a flush-mounted floating element mounted on a reactance gauge. The measured reactance was due to the shear caused by the flow. The reactance was used to transduce the displacement into wall shear force. The results show an agreement with the laminar flow of Blasius's solution and a fully developed turbulent flow over a flat plate. Currently, many of the design principles are similar but use much more advanced signal conditioning, which employs a high-resolution sensor.

1.4.2 Recent Developments of Floating Element Balance

As mentioned previously in the motivation section, the primary inspiration for this study is Ferreira et al.. They conducted the test in a subsonic wind tunnel with freestream velocity ranging from $10m/s$ to $26m/s$, increasing $2m/s$ after each measurement. Their results show an agreement with hot-wire anemometry measurements. They demonstrate the meticulous design of floating element balance, which is not only facilitated in measuring the wall shear stress but also the induced pitching moment caused by the wall shear. This careful consideration is due to the use of the classical parallel-linkage mechanism. In the Figure 1.9, the various components of the design are highlighted which are as follows: the floating frame, fixed-supported by a pair of flexures on the upstream side, which allows the floating frame to move freely, and a pair of aluminum blades 15 mm long, 10 mm wide, and 0.45 mm thick. A pair of holders are installed between the floating frame and the element, allowing the frame to rotate freely about the pivot point. Another pair of blades horizontally mounted on each side of the floating frame are used to counter the pitching moment.

The size of the floating element is 200 mm $\times$ 200 mm. All described components are assembled in an aluminum enclosure with outer dimensions of 220 mm $\times$ 220 mm $\times$ 40 mm. This enclosure is also compact enough to hold all the electronics inside. To mitigate the error contributions from the pressure differential acting along the non-parallel surface to the flow and misalignment of the floating surface with the fixed surface, they utilized a $15mm$ long S-shaped mechanical labyrinth seal with a lip thickness of $\lambda = 1mm \pm 0.1$ and a gap of $\gamma = 0.5mm \pm 0.1$. In addition, their design employs a centrifugal blower that modifies the pressure in the enclosure. Two nozzles were used, one near each non-flow side of the floating element. This feature guarantees uniform pressure distribution on the non-flow side of the floating element and maintains the pressure inside the enclosure.

The instrumentation in Ferreira et al. [23] consists of metal strain gauges installed on both sets of blades mentioned above that are connected to a custom-built acquisition module powered by a $5V$ supply. The acquisition module has the necessary signal conditing and filtering, which utilizes a low-noise $24 - bit\Sigma\Delta$ ADC. In addition, the device was calibrated in situ using a combination of weights and string-pulley setup. These static measurements were used to acquire a calibration curve.

Recent work of **Baars et al.** [3] shows another successful implementation of a large-scale floating element balance with a surface area of $3m$ $\times$ $1m$ in the streamwise and spanwise direction, respectively. This large surface area improves the measurement by minimizing the systematic errors associated with the measurements. Additionally, this also improves the overall signal-to-noise ratio of the measurements. However, a limitation of the design is that its moveable components have a total mass of $250kg$, which may cause difficulty in experimental logistics. They conducted the tests in a high Reynolds number wind tunnel facility, where the streamwise distance at which the floating element was mounted was $21m$, and the streamwise velocity was kept under $45m/s$. For smooth-wall, the freestream velocity

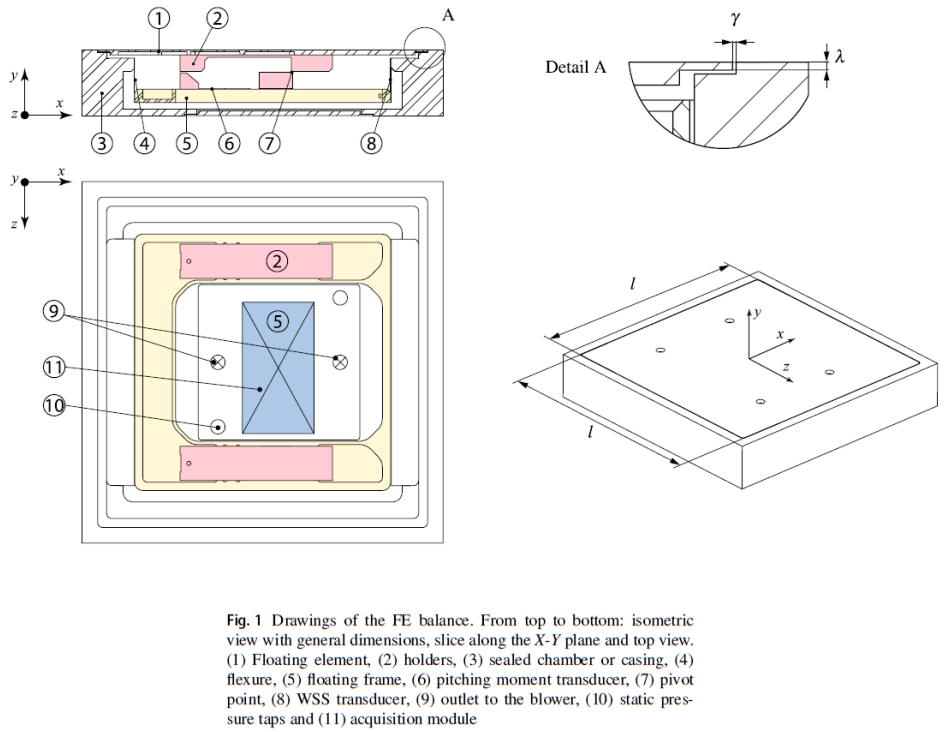


Fig. 1 Drawings of the FE balance. From top to bottom: isometric view with general dimensions, slice along the *X-Y* plane and top view. (1) Floating element, (2) holders, (3) sealed chamber or casing, (4) flexure, (5) floating frame, (6) pitching moment transducer, (7) pivot point, (8) WSS transducer, (9) outlet to the blower, (10) static pressure taps and (11) acquisition module

Figure 1.9: Schematics of the Floating Element Balance from Ferreira et al. [23]

ranges from $8m/s$ to $26m/s$, with increments of $2m/s$. The smooth-wall zero pressure gradient results show an agreement with the **Coles-Fernholz** relation, $C_f = 2\left(\frac{1}{\kappa}\ln(Re_\theta) + C\right)^{-2}$, where κ is the von Kármán constant, Re_θ is the momentum thickness Reynolds number, and C is an empirical constant.

The Figure 1.10 shows the design assembly of used in Baars et al., which features the surface area $3m^2$ for the floating element. The floating element is supported by a tubular steel frame with a cut-out in the middle for modular inserts, which can be replaced with a smooth wall or rough wall as desired. This tubular steel frame is supported and stabilized by four air-bearing assembling mounted at each corner. The air-bearings have a planar surface of $200mm \times 100mm$, operated with a pressure supply around $800kPa$. All of these components are assembled in a pressure-controlled chamber. The floating element is mechanically sealed via a complex labyrinth seal with a vertical gap of $0.7mm$ and a horizontal gap of $2.0mm$.

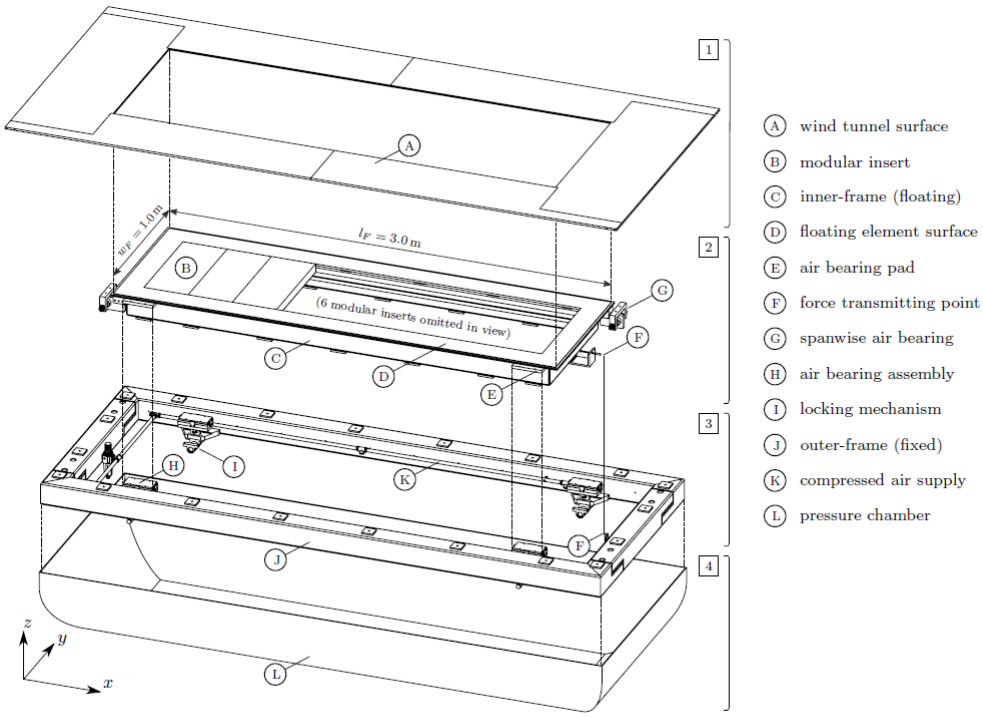


Fig. 4 Exploded view of the floating element assembly embedded in the test section of the Melbourne wind tunnel. The assembly is exploded in *vertical* direction (z-coordinate) in four stages in order to explicitly visualize subassemblies [*1*]–[*4*]

Figure 1.10: Assembly of the Floating Element Balance from Baars et al. [3]

.

The floating element is an integral component of the wind tunnel, which has a locking mechanism to ensure safety when not in operation. In addition, the air bearings allow a frictionless floating movement of the floating element. A positive tilt is designed in the surface from the streamwise direction, causing the floating element to return to its neutral position.

Consequently, this inclination also eliminates any excessive drift after a minor displacement from the wall shear, shown in Figure 1.11. This misalignment may cause a pressure differential across the floating surface, corrected by maintaining the pressure in the enclosure or subtracting the contributions of Δp from the wall shear force. For instrumentation, a single-beam load cell with a capacity of $6N$ is used to measure the force with a sampling rate of $1kHz$ and a $16-bit$ ADC. The load cell is statically calibrated before and after each

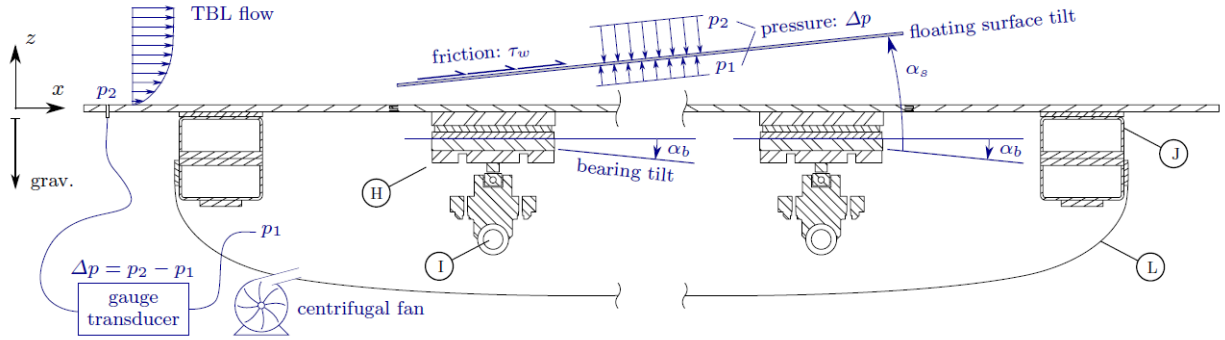


Fig. 10 Sectional view B–B, indicated in Fig. 7a (enlarged 2×), illustrating the air bearings, FE surface, wind tunnel floor and relevant misalignment angles. Labeled annotations are described in Fig. 4

Figure 1.11: Misalignment caused by the tilt in the air-bearings from Baars et al. [3]

.

measurement series to account for any drift in the output over time.

1.4.3 Inherent Errors Associated with the Measurement

There are many sources of errors associated with the floating element balance measurements, as mentioned by Winter [64]. However, this subsection will only discuss the inherent errors with this measurement as discussed by Allen [1, 2], Brown and Joubert [8], O'Donnell [45]. The description of the sources of the errors in floating element balance is as follows:

1. **Uneven Static Pressure Forces Acting Normal to the Element**

   The static pressure forces distributed across the floating element will cause the element to pitch. This pitching, coupled with the moment caused by the wall shear stress, will introduce errors in the measurements. The effects of uneven static pressure distribution are very high in a single-pivot floating element as compared to a parallel-linkage mechanism. In a non-zero-pressure gradient measurement, the impact of this type of error is significant.

2. **Static Pressure Forces on the Edges of the Element**

   The static pressure forces interacting with the edges of the floating element (such as the leading edge) will cause an overestimation of the measurements due to the contribution of these forces.

3. **Disturbance due to the Surrounding Gap**

   The disturbance caused by the surrounding gap around the floating element causes cavity-induced flow, which generates a pressure gradient between the non-flow side and the flow side of the element.

4. **Misalignment of the Floating Element**

   The misalignment of the floating element means that it is not flush-mounted with the fixed surface. This misalignment can be due to protrusion or recession of the element. Misalignment is perhaps the most influential cause of measurement inaccuracy.

The contributions of these errors are coupled together [8], which can cause erroneous measurements. For instance, **(4)** misalignment would mean that the floating element is either protruding or recessing, which would give rise to **(2)** and **(3)**. This combination will cause the measurements to be overestimated as it will have contributions from the lip forces and pressure gradient between the flow-exposed side and the non-flow side of the element. This will have a significant impact if the balance uses single-pivot as it will introduce **(1)**.

The analysis by Brown and Joubert shows the details of **(2)** and **(3)**, where the wall shear stress has erroneous contributions from the pressure force on the edge of the element by the streamwise pressure and the pressure differences on both sides of the element. **(2)** can be

mathematically written as $F_p = -C_1\,\varepsilon\,\rho\,\alpha S$, where F_p is the pressure force on the edge, C_1 is a constant (expected to 0.5), ϵ is the effective element edge height, α is the kinematic pressure gradient as described in Brown and Joubert [8] ($\alpha = \frac{1}{\rho}\frac{\partial p}{\partial x}$), ρ is the density and S is the surface area of the floating element. In a pressure gradient, the total pressure force on the element will oppose the direction of the pressure gradient. The contributions from **(3)** are caused by the pressure difference between the flow-exposed side and the non-flow side in the enclosure of the floating element balance. The flow penetrating from the high-pressure side of the enclosure and exiting from the low-pressure side of the element will result in a momentum exchange, and a part of this will be transferred to the floating element. By examining the surrounding gap, this momentum force can be mathematically written as $F_m = C_2\rho g S\alpha u_\tau^2$ as described in [8], where C_2 is a constant of unknown magnitude, g is the gap width and u_τ represents the frictional velocity because this is a momentum exchange near the wall.

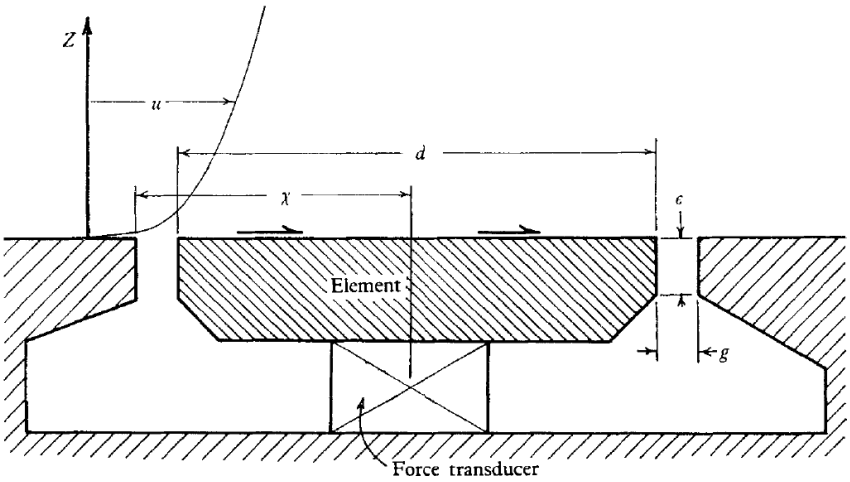


FIGURE 2. Floating-element shear stress meter principle.

Figure 1.12: Principle of Floating element balance from [8]. Where Z is the wall-normal height, u is the streamwise velocity, χ is the distance from the pivot center of the element to the fixed surface, d is the diameter of the element, ϵ is the element edge height, and g is the gap width.

The error contributions of **(4)** was first studied by O'Donnell. The testing consisted of

incremental protrusion of $0.0006in$ using a lead screw, which allowed the translation of the balance while keeping the flow conditions constant. The results of the study show general agreement with previous studies, which did not employ finer misalignment using a traversing mechanism. Years later, Allen conducted a systematic study that addresses **(1)** and **(4)**. Allen varied the gap size and the misalignment of the element by protruding it using an adjustable drive mechanism. The design consisted of a moment-measuring single-pivot floating element balance. Any rotation due to a force-induced moment is countered by an electrically generated force, which creates an equal and opposite moment. The output voltage required to keep the sensing element neutral is used to infer the friction force (if perfectly aligned). The total force can be expressed as the sum of the coefficient of lip force C_L on the edge of the element, the coefficient of the normal force C_N on the surface of the element, and the coefficient of the friction force C_F.

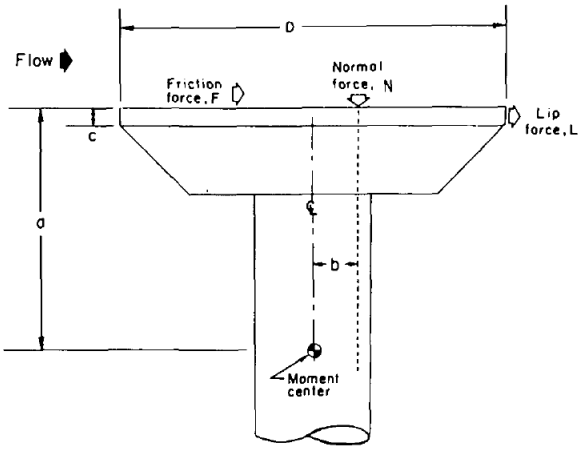


Fig- 1 Aerodynamic forces acting on element

Figure 1.13: Empirical relationship for floating element balance from Allen

$$C_T = C_F + \left(1 - \frac{c}{2a}\right) C_L + \frac{b}{a} C_N \tag{1.29}$$

The total force coefficient (Equation 1.29 is normalized by dynamic pressure and area) is

used to normalize the skin friction, and in the condition where the protrusion is zero and the ratio of $\frac{C_F}{C_T}$ is close to 1 is considered where lip force and normal force is negligible. For the protrusion study, a dummy sensing element was used to measure each of these forces individually. A dummy sensing element with pressure ports on its lip with 22.5° spacing covering the rim of the element was used to measure the lip force. A dummy sensing element with pressure ports covering 14 different radial locations on its flow-exposed surface was used to approximate the normal force. To obtain the pressure distribution on the surface of the element, it was rotated in small increments. Finally, for skin friction, they employed a Preston tube on a dummy sensing element to infer the skin friction.

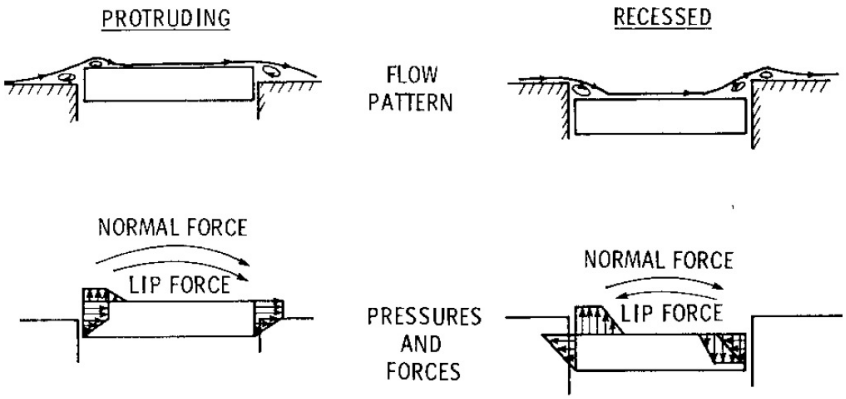


Fig. 2 Misalignment effects on sensing element.

Figure 1.14: Misalignment of floating element balance from Allen

The value of friction force from the ideal conditions where the lip and normal forces are negligible (at zero protrusion) is considered the total force. This total force is used as a benchmark for varying the protrusion and gap size. The effects of protrusion on lip forces reveal that for positive protrusion, the upstream pressure was higher than the downstream pressure, which resulted in a positive lip force. Meanwhile, for negative protrusion, the downstream pressure was higher, creating a negative lip force. As expected, at zero protrusion, the lip forces were negligible. The lip forces are also sensitive to the gap size. The lip

forces were higher at small gap sizes with a higher protrusion, indicating that increasing the gap size would reduce the effects of lip force in the case of a large protrusion. The effects of protrusion on normal forces would cause an uneven pressure distribution, and the resultant normal force would act off-center, inducing a moment that can introduce other sources of errors (as described in subsection 1.4.3). The results reveal that with a negative protrusion, the leading edge had a low-pressure distribution, while the trailing edge had a high-pressure distribution. This would cause a substantial contribution to the overall output.

Furthermore, the comparison between the forces reveals that the contribution from the lip forces and normal is substantial when the element is misaligned. Even a small protrusion can cause large magnitude of these forces. This study highlights careful design choices and precise engineering of the components. Although the empirical relationship used in [1] pertains to this design, the underlying experimental method can be applied to obtain a specific relation for different designs. Another work of Allen reveals that the effects of decreasing the lip thickness would virtually remove lip forces **(2)**, and employing a parallel-linkage mechanism would remove the normal forces **(1)**. Other studies, such as Frei and Thomann, Hirt et al., utilize a pool of liquid in the gap surrounding the element, which deals with reducing the effects of **(2)** and **(3)**. However, this is not always feasible for large-scale applications.

1.5 Scope of Research

Skin friction measurement is already complex without introducing the experimental logistics. The methods of measurement mentioned in this study have their advantages and limitations. They mainly depend on the application and compatibility. The indirect methods, such as the flow about an obstacle and Clauser estimation (described in subsection 1.3.1), are easy to use. However, the accuracy of results is compromised in the presence of complexities

as described in [8, 20, 36]. Since these methods require assumptions about the flow, this relationship would also change with introducing complexity. They require careful correction or calibration, which is hard to achieve without experimentation.

In contrast, direct methods do not rely on such assumptions, so they perform well in complex flow conditions. OFI (described in section 1.3.2) is one of the most robust direct measurement techniques[21, 65], but it has complex experimental logistics[13, 35]. Similarly, the MEMS-based sensor (described in section 1.3.2) can be used in complex conditions[43], however it has difficult calibration[61]. Alternatively, the floating element balance can be used in adverse pressure gradients. However, intricate design expertise is required to gain accurate measurements in such conditions (as discussed in the section 1.4). The floating element balance performs well in rough walls (demonstrated by studies such as [3, 23]), whereas OFI is incompatible with roughness. Floating element balance calibration can be conducted without a testing facility by installing it in a simple and stable structure, making it even more convenient. These necessities make the floating element balance a promising option for complex flow conditions and roughness studies. However, the floating element also has a few limitations, as mentioned in subsection 1.4.3, which can be minimized with careful design choices and expertise.

With the above-mentioned concerns, it is essential to study how floating element balance can be implemented in the Stability Wind Tunnel at Virginia Tech. Therefore, the objectives of this work are as follows:

1. Understand the constraints and requirements of the SWT to develop the floating element balance.

2. Understand how floating element balance can be developed for a side wall of the testing facility.

3. Design the components of the floating element balance.

4. Design and analyze a low-cost force transducer capable of detecting a small magnitude of forces.

5. Collect data to calibrate and record the response of the balance.

6. Conduct preliminary experiments in a pilot test facility to evaluate the feasibility of the device in the SWT.

Chapter 2

Design Configuration

The literature review discussed the design of [23] and inherent errors in the measurement (described in subsection 1.4.3), which emphasizes that a parallel-linkage mechanism is most suitable to minimize the intrinsic errors. Following the details from subsection 1.4.2, this section will present the details of the design used in this study, components of the prototype, mechanical analysis of the design, and details about the force transducer.

2.1 Mechanical Configuration

The floating element balance is designed for the modular insert test section configuration. The modular inserts for the Stability Wind Tunnel use a $609.6mm \times 609.6mm$ aluminum panel with $4.8mm$ thickness for simple installation [22]. The primary motivation for the designed is to be installed on one of such panels for ease of installation. Recent studies, such as [9, 10, 17], have used this modular insert configuration by utilizing the port-side wall of the test section.

The balance is designed to supplement the studies conducted on the side walls. The floating element balance is intended to measure the streamwise wall shear stress, allowing it to be displaced only in the streamwise direction; the design features a constrained parallel linkage system that behaves similarly to a linear oscillator. The balance is enclosed in a 3D printed enclosure with dimensions of $280mm \times 330mm \times 265mm$. The parts of the prototype were $3D$ printed using ABS material (shown in Figure 2.2). The mechanical configuration comprises two mounting frames $228mm \times 228mm \times 43mm$, a floating frame $203mm \times 203mm \times 203mm$), eight flexure supports, an aluminum floating element, and a counterbalancing plate. The design features a parallel linkage mechanism using stainless steel flexure, which acts as a compliant mechanism. The floating frame is mounted using eight flexure supports on the mounting frames, with four on the upstream side and four on the downstream side. The floating element and its counterbalance are mounted on the floating frame using four countersink screws. The counterbalance plate is required to keep the frame steady. In the absence of the counterbalance plate, the floating element will cause instability.

The combination of eight flexures allows the floating element to be sensitive to the streamwise load while resisting normal forces that act on it to resist the misalignment. As the floating element is displaced from its neutral position, the stiffness of these flexures will cause the floating frame to return to its neutral position, making it a non-nulling type of floating element balance. In comparison, The nulling types of floating element balance have a specialized mechanism that initiates a counteractive force to keep the floating element steady, making it much more efficient but complex to design and implement. The thickness of the flexure supports is very important since a thicker flexure will increase the stiffness, thus reducing the sensitivity of the balance to the streamwise load. The flexures are $50mm$ long and $20mm$ wide with a thickness of $50\mu m$. The top flexure on the upstream side near the floating

element is equipped with metal strain gauge to transduce the strain into the force caused by the displacement of the floating frame. The floating element area is $201mm \times 201mm$ with a lip thickness of $2.1mm$, with a surrounding gap of $1.8mm$ and $30mm$ long labyrinth seal between the fixed and floating surface. The gap between the floating element and the fixed surface is $\approx 1.8mm$ as presented in Figure 2.1.

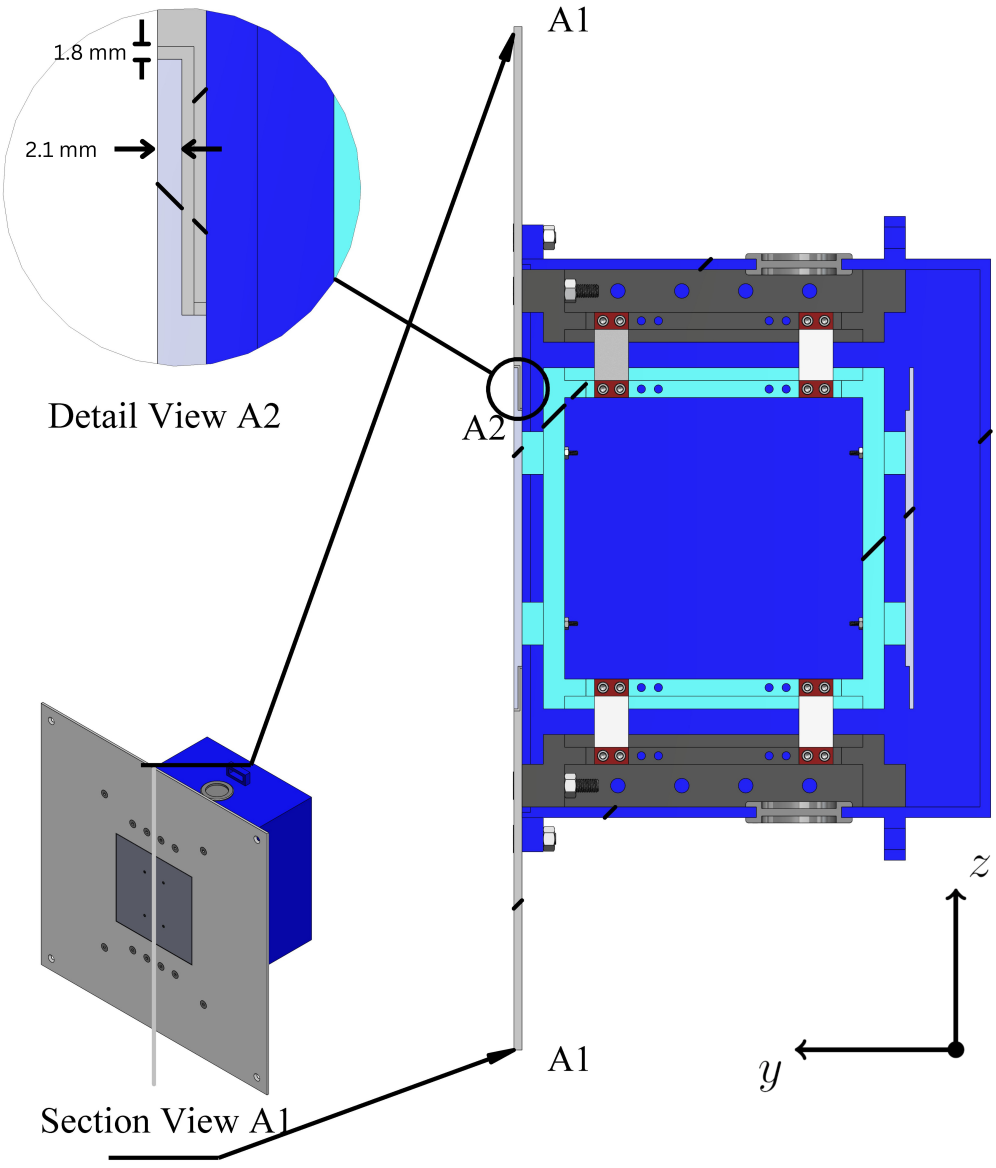


Figure 2.1: Section View A1: Floating element balance assembly with the $3D$ printed prototype (blue: Enclosure for the balance). Detail View A2: $h_{gap} = 1.8mm$ and $h_{lip} = 2.1mm$

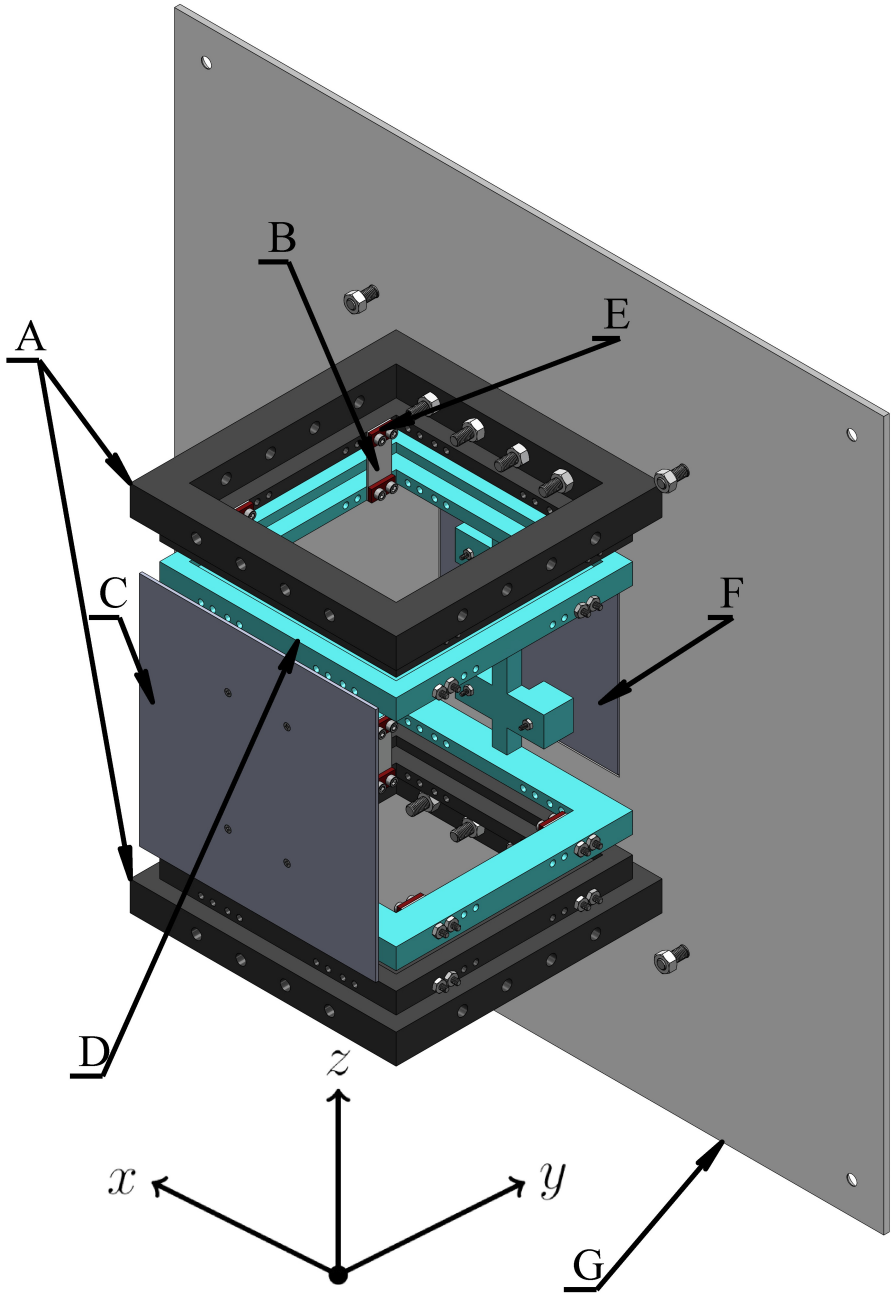


Figure 2.2: Components of the floating element balance: (A): mounting frames, (B): flexure (position of the strain gauge), (C): counterbalancing plate, (D): floating frame, (E): flexure mounting brace, (F): floating element (shown from the non-flow side), and (G): aluminum panel rigidly fixed (enclosure hidden in the assembly)

2.2 Mechanical Analysis

Compliant flexures generally have a high slenderness ratio, so the displacement of the floating element can be estimated using the Euler-Bernoulli beam theory to find approximate deflection in the compliant mechanism. The assumptions for this mathematical modeling are as follows: The floating frame is fixed rigidly with the flexures, the floating frame moves rigidly due to the wall shear force, the axial forces acting on the flexures are negligible, the shear deformation due to the induced pitching is minimal, the deflection in the flexures are approximately equal, and the maximum deflection in the flexures is equal to the maximum displacement of the floating element. The flexures can be modeled as a fixed-on-both-ends beam with lengths $2L$ with a central point load equal to $\tau_w S/2$ (the magnitude is half because there are a pair of flexures on both sides), where S is the surface area of the floating element $S = L_{FE} \times W_{FE}$. The thickness and width of the compliant flexures are t_{cm} and W_{cm} respectively. So, The second moment of inertial of the beam can be calculated by:

$$I_{cm} = \frac{W_{cm} t_{cm}^3}{12} \tag{2.1}$$

The deflection of a fixed-on-both-ends beam with a central point load can be represented as:

$$\Delta_x = \frac{PL^3}{192EI} \tag{2.2}$$

Substituting the values for $P = \tau_w S/2$, $L = 2L_{cm}$, $I = (1/12)W_{cm} \times t_{cm}$, E is the elastic modulus of steel equals to $210GPa$, the maximum deflection can be defined as:

$$\Delta_{x\max} = \tau_w \frac{L_{FE} W_{FE}}{4EW_{cm}} \left(\frac{L_{cm}}{t_{cm}}\right)^3 \tag{2.3}$$

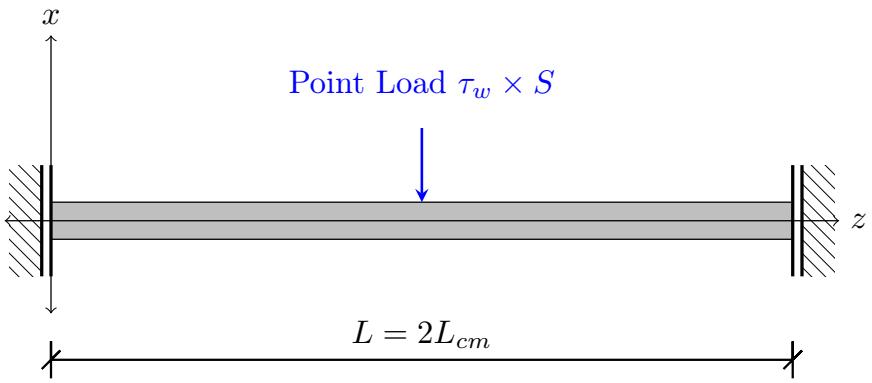


Figure 2.3: Modeling of the compliant flexures as beam fixed on both ends with central point loading caused by the wall shear force

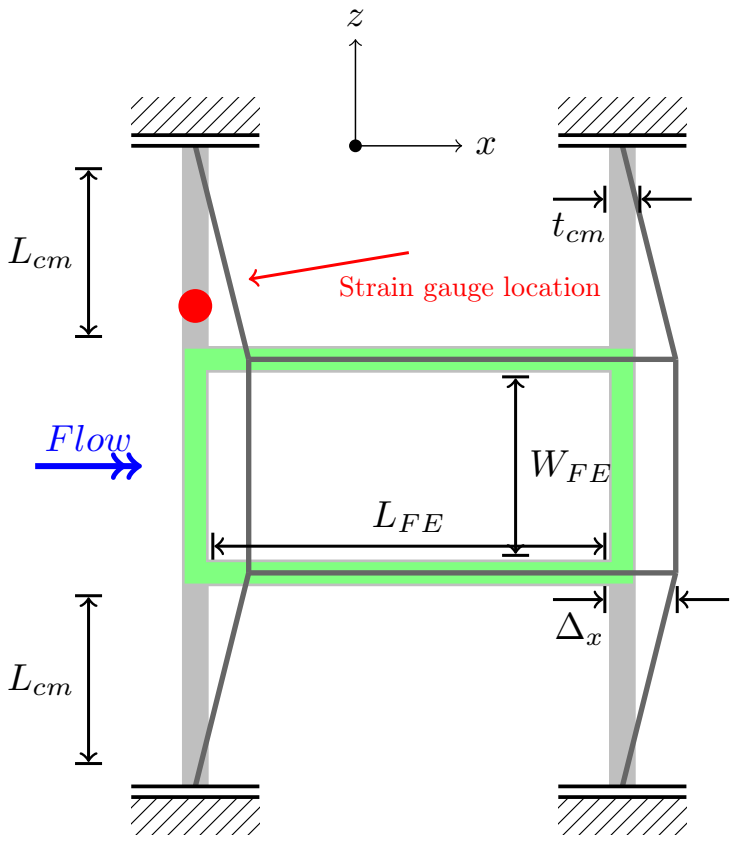


Figure 2.4: Diagram of displaced floating element due to the flow and deflection in the compliant mechanism (flexures), red dot represents the location of strain gauge $\approx L_{cm}$ - (Front View)

Using the force-deflection relationship, the stiffness of the compliant mechanism will be as follows:

$$k_{cm} = \frac{4EW_{cm}}{(\frac{L_{cm}}{t_{cm}})^3} \tag{2.4}$$

The floating element balance can be modeled as a spring-mass system to determine its natural frequency. The combined mass M_{asm} of the floating frame, sensing element, and counterbalance plate is approximately equal to $1.1kg$. The natural frequency is ≈ 2.8 Hz.

$$f_n = \frac{1}{2\pi}\sqrt{\frac{k_{cm}}{M_{asm}}} \tag{2.5}$$

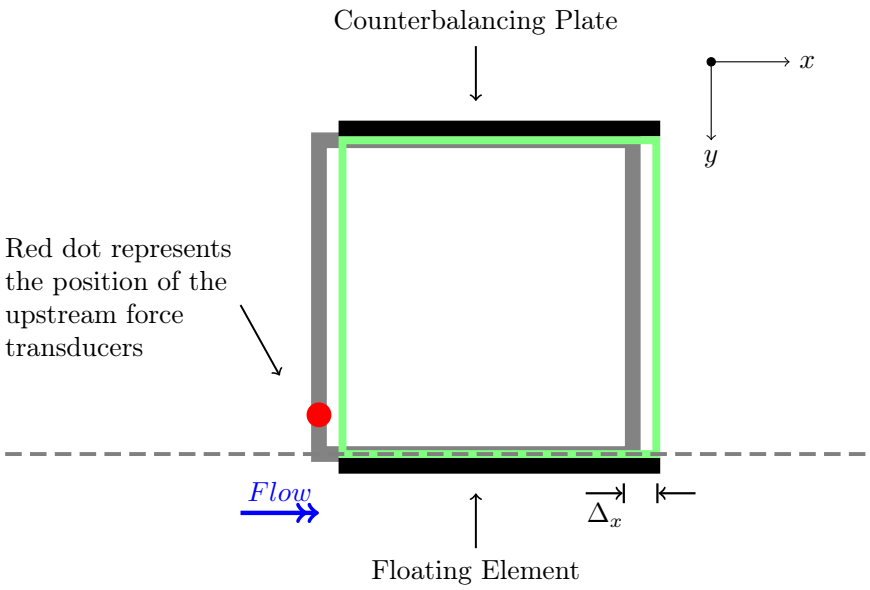


Figure 2.5: Diagram of displaced floating element due to the flow and deflection in the compliant mechanism (flexures), red dot represents the location of strain gauge $\approx L_{cm}$ - (Top View)

The total strain in all the flexures can be approximated with the relationship of the bending

normal stress at L_{cm}, assuming all the flexures have equal strain. The strain can be represented as Equation 2.6, where F_w is the central point load applied on the floating element balance [16].

$$\varepsilon_{cm} = \left(\frac{F_w L_{cm} \cdot t_{cm}}{32 E I_{cm}} \right) \tag{2.6}$$

2.3 Strain Measurements

Strain gauges are popular with compliant flexures, mainly used to transduce displacement or strain into force. One of the more popular configurations of strain gauges is the full bridge strain gauge. The full bridge strain gauge circuit consists of four equal resistances of thin metallic wire carefully designed to detect the slightest change in its electrical resistance on account of tension or compression. The full bridge circuit is excited typically with a constant voltage $V_{exc} = 5V \ to \ 10V$, the excitation voltage V_{exc} is applied across the pair of opposite nodes, and the differential voltage out at the two remaining nodes is measured. At zero load, therefore, no compression or tension, the bridge will be balanced, and the voltage output will be zero, which means no strain. But as the force is applied, it will change the resistance in the bridge, resulting in a non-zero V_{out}. This is due to the relationship between resistance and the material properties defined as:

$$R = \rho \cdot \frac{L}{A} \tag{2.7}$$

Where R is the resistance of a thin wire, ρ is the density of the wire, L is the length of a wire, and A is the cross-sectional area of the wire. An increase in length will increase the resistance of a wire. For most applications, this relationship will remain mostly linear.

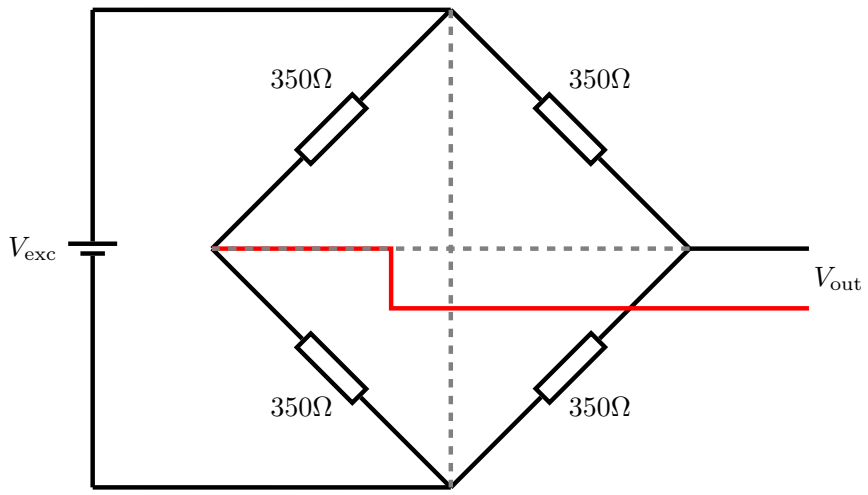


Figure 2.6: Diagram of the full bridge strain gauge V_{exc} is the excitation voltage and V_{out} is the signal output

The Figure 2.6 shows that a full-bridge strain gauge circuit, which acts as a force transducer, was installed on the flexure at $\approx L_{cm}$. This flexure was installed at the top of the upstream side Figure 2.4 and Figure 2.5. As the floating element is displaced, the full bridge strain gauge will become unbalanced, and a non-zero voltage output will represent the strain in the flexure. The output voltage from the full-bridge strain gauge has a relationship with the strain defined as Equation 2.8, where G_F is the gauge factor of strain gauge (for metal gauges ≈ 2), and ε is the strain [5, 32, 42].

$$\frac{V_{out}}{V_{exc}} = G_F \cdot \varepsilon \tag{2.8}$$

A series of data was collected using different loading conditions to understand the relationship of force-strain in the floating element balance. The floating element balance was installed on an extruded aluminum frame with a string-pulley configuration. The pulley PASCO $ME - 9448b$ was used for this purpose, with a diameter of $50.8mm$, an approximate mass

of $5g$, and an effective coefficient of friction 7×10^{-3}[23]. For signal conditioning and data acquisition, HGL Hummingbird was used (as described in section 3.3). The purpose of these static measurements was to assess the stability of the balance. The balance was assembled before the measurements and disassembled after the measurements. These measurements were taken over a four-week period, with intermittent data collection to assess the long-term performance of the balance. Measurements were obtained across selected days throughout this evaluation interval, enabling a comprehensive assessment of the force transducer over an extended period. The balance was loaded with various weights ($2g$, $3g$, *and* $5g$) interval to understand the voltage output Figure 2.8.

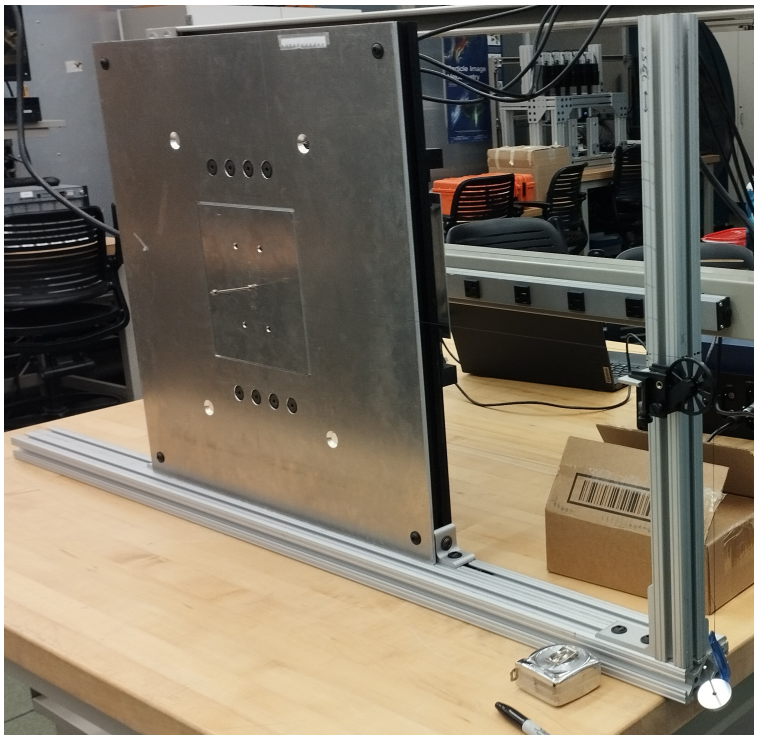


Figure 2.7: Floating element balance mounted on extruded aluminum for the study of strain behavior in the flexure.

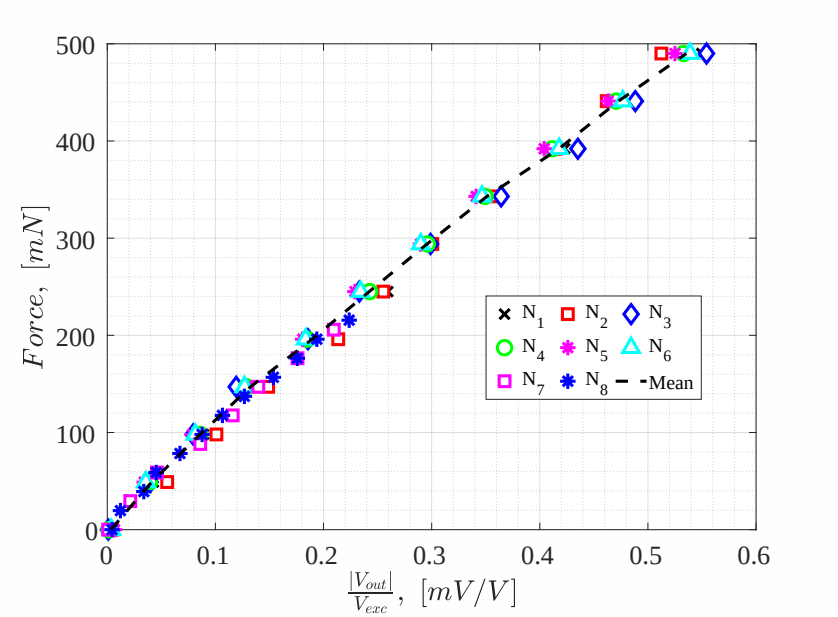


Figure 2.8: Voltage readout from the balance, where N_i is the data series and i represents the number of series. – – $\frac{|\overline{V_{out}}|}{V_{exc}}$: mean of the N_i series.

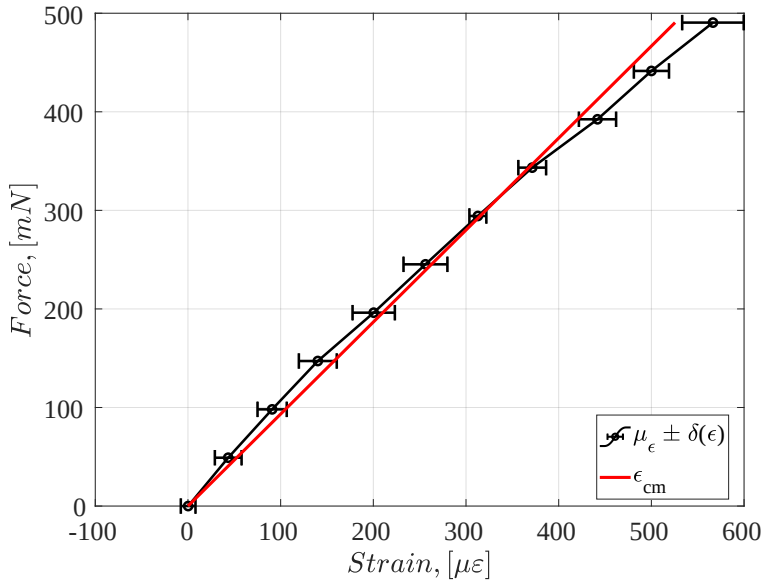


Figure 2.9: — ε_{cm}: calculated strain from Equation 2.6. — μ_ε: mean of the N_i series and error bars show the measurement uncertainty in the mean represented by $\pm\delta(\epsilon)$

The floating element has an hole in the center for a stud, which is tied with a thread and looped around the pulley once to hang weights Figure 2.7. The thread is parallel to the surface, emulating the wall shear force F_w. The balance was loaded with weights (e.g., $(5g - 50g) \times 9.8m/s$). The data was recorded at $250kHz$ for $30s$ to ensure convergence to the mean for a short sample duration. Since these measurements were taken under static conditions, a high sample rate would improve the mean value by sampling a higher number of the fluctuating values. The mean values of these independent measurements are presented in Figure 2.8. The measurements are taken from one of the flexures Figure 2.5. However, assuming the strain is of similar magnitude in the other downstream flexures (because equal EI_{cm}), so multiplying the strain acquired from one set of full-brdige with a factor of 2, it can be compared with the calculated total strain ε_{cm} Equation 2.6 as presented in Figure 2.9.

As shown in the Figure 2.9, the blackline (—) for μ_ε shows a non-linear behavior at $\approx 0 - 200mN$, which gradually becomes linear at higher forces. The strain ε_{cm} calculated from the Euler-Bernoulli beam theory lies within the error bar in the non-linear region of the measured strain until 400 mN. The uncertainty $\delta(\varepsilon)$ at around $500mN$ is 4% to the experimental mean μ_ε. The model ε_{cm} assumes the strain approximation at the center of the fixed-on-both-ends beam model and assumes homogeneity in the material, ideal loading, and boundary conditions. In contrast, the experimental strain and approximation is due to the location of the strain gauge at $\approx 0.7L_{cm}$, non-homogeneity in the flexure material, sensitivity of the strain gauge, and uneven loading conditions in the flexures. For general comparison, the model ε_{cm} shows an agreement with the experimental strain. The variations at higher loads suggest additional effects are not captured by the assumptions in Euler-Bernoulli beam theory, such as the flexures rigidly fixed and rigid movement of the floating frame. However, the magnitude of the error margin remains small even at higher loading conditions, proposing that this model captures the overall behavior very well.

2.4 Geometric Inconsistencies

The gap between the floating element and the fixed surface was designed to be at $\approx 1mm$, but due to some irregularities in the machining process, such as an offset of $\approx 3mm\ to\ 5mm$ in the middle square cut out. This caused the surrounding gap to be uneven, with an average of $\approx 1.8mm$. The aluminum panel with the dimension of $609.6mm \times 609.6mm \times 4.8mm$ is a cold-rolled aluminum sheet was not perfectly flat before the machining process. The $3D$ printed prototype, specifically the floating frame, also had a few inconsistencies in the geometry, such as the mounting points of the floating element had a slightly uneven edge, sanded and smoothed out using coarse sandpaper. These inconsistencies caused the floating element to be misaligned by a protrusion of $\approx 1.2mm\ to\ 2mm$.

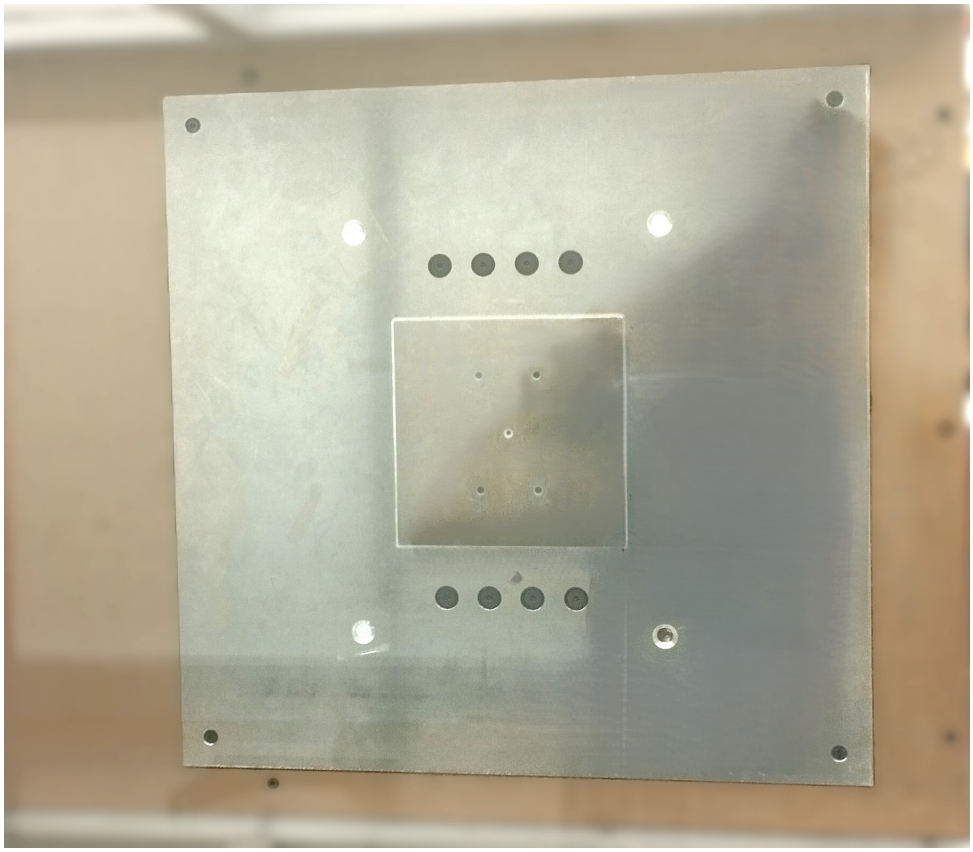


Figure 2.10: Fixed aluminum panel for the floating element balance

Chapter 3

Experimental Facility and Instrumentation

3.1 Open Jet Subsonic Wind Tunnel at Virginia Tech

The open-jet subsonic wind tunnel facility is located at the Goodwin Hall of Virginia Tech. The open-jet wind tunnel structure consists of a steel frame foundation with aluminum panels and an extruded aluminum frame for stability. The flow speed of the blower is controlled by an AF-600 GE variable frequency drive. The flow for the tunnel is powered by a 30-horsepower BC-SW Size 365 Twin City centrifugal blower capable of generating flow rates up to $15m^3/s$. The blower output is channeled into a 6° and $4m$ long diffuser. The flow is directed into a $1.47m \times 1.78m$ settling chamber height and width, respectively. After which, the flow is passed through a combination of honeycomb with $0.01m$ cell size and $0.09m$ long followed by three different turbulence screens with $0.3mm$ diameter fiberglass with an open area ratio of 55%. Finally, the flow is passed through a 5^{th} degree polynomial curved contraction nozzle with an area ratio of 5.5 to 1, where the flow is discharged into

the atmosphere. The exit area of the contraction is $0.71m \times 0.71m$, where an aluminum extruded structure is used as a test section. Alternatively, a modular closed test section with the dimensions $0.71m \times 0.71m \times 1.21m$ is utilized for this study. The walls of the closed test section are made of $0.35in$ thick acrylic panels mounted in the test section using countersink bolts. A jet catcher is installed after the test section, which is made of fiberglass screens and an extruded aluminum frame with composite panels. The flow is defused and deflected in this jet catcher, which reduces the impact of the flow in the lab. The freestream velocity of the flow is calculated by sensing settling chamber pressure using *Pressure Scanner* 9816 $\pm$ $10in\ H_2O$ ($\pm 0.05\% FS$). The atmospheric pressure and temperature are measured using a digital barometer/thermometer $Model\ DBT - 100T$. The freestream flow conditions are displayed on the MATLAB GUI.

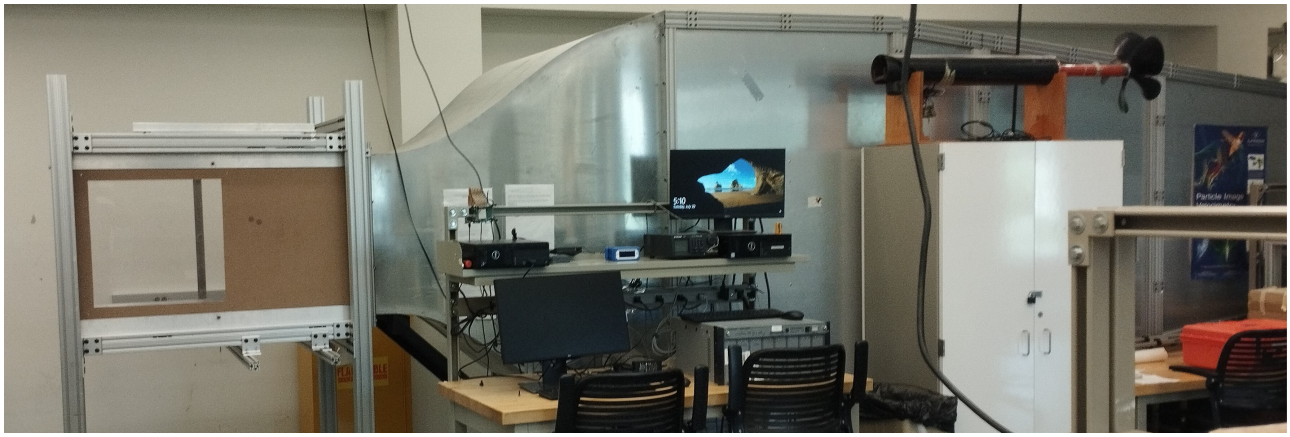


Figure 3.1: Subsonic Open Jet Wind Tunnel with modular closed test section

3.2 Experimental Setup

The modular closed test section was used for wall shear measurement. To create a seal between the contraction of the wind tunnel and the closed test section, a $0.5in$ wide foam tape was used to prevent flow leaks. The starboard acrylic panel of the closed test section



Figure 3.2: Modular Test Sections of Open Jet Wind Tunnel: open(Left) and closed(right)

was replaced by an MDF panel with a machined cutout for the aluminum panel. The floating element balance was assembled on the aluminum panel for the wall shear measurements in a steady flow. The calibration data was acquired before and after the measurement session. The floating element balance is $\approx 0.76m$ from the contraction. Due to some uneven edges in the MDF panel, plastic tape was used to seal the uneven edges to prevent the flow from leaking.

3.3 Data Acquisition System

The data acquisition system used for the direct wall shear measurements is HGL Dynamics Hummingbird. The Hummingbird DAQ is enclosed in a robust casing, supplemented with fins around the casing for efficient cooling. The Hummingbird DAQ features 48 input channels, each incorporating a $24 - bit\Sigma\Delta$ analog-to-digital converter. The input range of the signal is $1V\ to\ 10V \pm 0.1V$. The DAQ is instrumented with a gain amplification of $\times 500$ with $120dB$ SNR and a sampling rate of $250kHz$, with a $100kHz$ of stable anti-aliasing band-

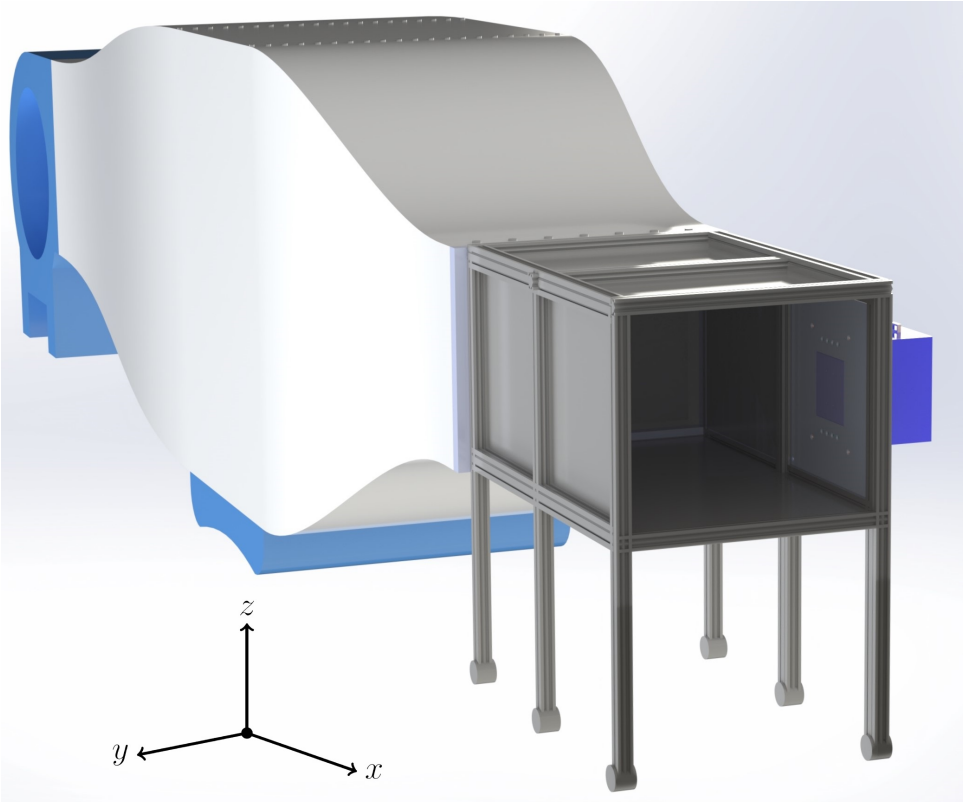


Figure 3.3: CAD of Subsonic Open Jet Wind Tunnel with closed test section (not to scale)

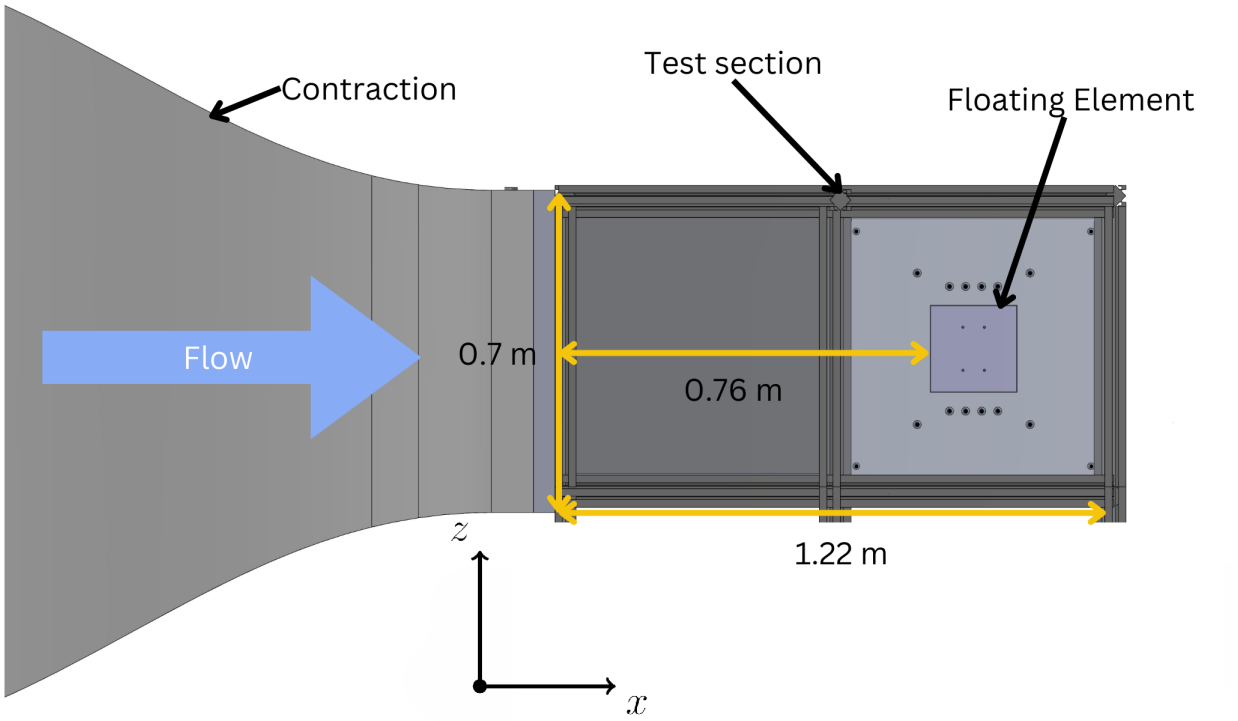


Figure 3.4: Side schematic view of the closed test section (not to scale)

width. The in-house built force transducers are connected through $8-pin$ LEMO connectors. HGL Hummingbird utilizes a Gigabit Ethernet connection to the dedicated computer. The computer runs the operating software that records and labels the data, providing a robust data acquisition.



Figure 3.5: HGL Dynamics Hummingbird DAQ

3.4 Static Response of the Floating Element Balance

The Figure 3.6 shows the static response of the balance with noise reduction mode. The balance was assembled and mounted on the extruded aluminum frame Figure 2.7, and a force of $\approx$ $500mN$ was applied using the string-pulley configuration for 5 $minutes$, then the force was removed, and the balance was allowed to be stable before the data was sampled for $\approx$ 15 $minutes$ sampled at $20kHz$ to observe the drift and hysteresis in the strain gauge. These measurements were conducted on three separate days over two weeks. The static response shows a drift in the response over time, which is significant in the redline (—) with almost 10% by averaging the samples for the first minute and the last minute to calculate the relative drift, while for blue (—) and green (—), it is under 2%. This drift response test raises a critical concern. More independent measurements are required to improve the confidence in the drift percentage over more extended periods of time. Since drift is bound to happen, it is crucial to stabilize or account for the drift. Failure to stabilize the drift would lead to increased uncertainty in the data due to the accumulation of the drift error, and the system would require more frequent calibration. The effects of drift can be minimized by utilizing filtering algorithm techniques.

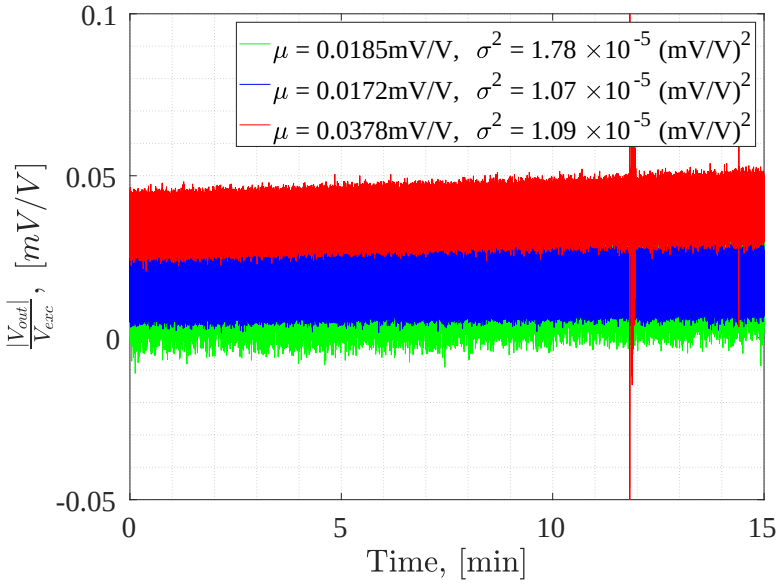


Figure 3.6: Drift in the static response of the force transducer using noise rejection mode. (—) has almost 10% relative drift, indicating an unstable drift, while (—) and (—) have under 2%.

3.5 Uncertainty

Uncertainty is defined as an error in the measurements due to imperfect conditions and unknown parameters. The uncertainty in the data is due to systematic constraints present in the system due to non-ideal conditions in material, dimension, and instrumentation. Repeated measurements provide a value for uncertainty with much higher confidence. Uncertainty is inherent in the system due to random error and system error. The uncertainty for a repeated measurement is defined as:

$$\delta(\overline{R}) = 2\frac{\sqrt{\frac{1}{N-1}\sum_{i=1}^{N}\left(R_i - \bar{R}\right)^2}}{\sqrt{N}} \tag{3.1}$$

Where R is the measured quantity, the numerator of the equation represents the standard

Table 3.1: Primary uncertainties in the measurement

Quantity	**Uncertainty (95% Confidence Interval)**
P_∞	0.05% to the full-scale
P_{atm} (Pa)	10
T (K)	0.5
ρ (kg/m^3)	1.9×10^{-3}
μ $(Pa \cdot s)$	2.4×10^{-8}

deviation for the measurement, N is the number of samples, i is the number of observations of the measurement, $\bar{R}$ is the mean of the measurement, and 2 represents the factor rounded up from 1.96 for 95% confidence in the measurement [28]. The Equation 3.1 is used to find the uncertainty in the strain measurement presented in Figure 2.9 and Figure 4.3.

For calculating uncertainty where two or more measurement quantities are involved, an assumption is made such that there is no systematic error present in the measurement, such as a bias. Uncertainty propagation refers to the combined uncertainty in the measurement due to two or more measured quantities. For uncorrelated uncertainties in the measurement, the uncertainty propagation is defined as:

$$\delta(R) = 2\sqrt{\left(\frac{\partial R}{\partial a}\delta(a)\right)^2 + \left(\frac{\partial R}{\partial b}\delta(b)\right)^2 + \left(\frac{\partial R}{\partial c}\delta(c)\right)^2 + \dots} \tag{3.2}$$

Where R is the measured quantity or a function, the partial derivatives with respect to the input variable represent the sensitivity coefficient, the $\delta(\ )$ represents the uncertainty in the input quantity, and 2 represents the factor rounded up from 1.96 for 95% confidence in the measurement [28]. The Equation 3.2 is used to find the uncertainty in Figure 4.9.

Chapter 4

Experimental Method and Measurements

4.1 Calibration Procedure

The calibration process is similar to what is described in section 2.3. The calibration data was acquired using a string-pulley configuration by loading the balance in situ with weights $[(0g,\ 3g,\ 6g,\ 12g,\ and\ 24g)\ \times\ 9.8m/s]$, with a string tied to a wall-normal stud installed on the floating element. The pulley was carefully mounted on an extruded aluminum frame to ensure that the force from weights would emulate wall shear stress. The Super Pulley by PASCO $ME-9448b$ has an approximate mass of $5g$, a diameter of $50.8mm$, and an effective coefficient of friction 7×10^{-3}[23]. The static data for these measurement points was obtained before and after the wall shear measurements. Four sets of calibration series were acquired before the wall shear measurements, and three were obtained after the measurements. The voltage output from the strain gauge was sampled for $60s$. This sampling duration was deemed sufficient since the balance is loaded statically to achieve significant samples, which

will converge to the mean and average out the noise.In total, 35 measurement points were acquired to achieve statistical significance, 7 for each weight point, which increases the confidence in the calibration data. These 7 repeated measurements for each of the weights were used for ordinary least squares. The linear regression is described as Equation 4.1, where y is the force, β_1 is the slope of the linear fit, x_1 is the mean voltage values, β_0 is the intercept of the linear fit, ϵ_{RE} is the residual error term.

$$y = \beta_1 x + \beta_0 + \epsilon_{RE} \tag{4.1}$$

The equation Equation 4.1 can be expressed in the matrix form as following, where N_{i_j} represents the data points of the series, i represents the series , and j represents the point relative to the force value:

$$\mathbf{y} = \begin{bmatrix} y_{N1_1} \\ y_{N2_1} \\ y_{N3_1} \\ y_{N4_1} \\ \vdots \\ y_{Ni_j} \end{bmatrix}, \quad \mathbf{X} = \begin{bmatrix} x_{N1_1} & 1 \\ x_{N2_1} & 1 \\ x_{N3_1} & 1 \\ x_{N4_1} & 1 \\ \vdots & \\ x_{Ni_j} & 1 \end{bmatrix}, \quad \beta = \begin{bmatrix} \beta_1 \\ \beta_0 \end{bmatrix}, \quad \begin{bmatrix} y_{N1_1} \\ y_{N2_1} \\ y_{N3_1} \\ y_{N4_1} \\ \vdots \\ y_{Ni_j} \end{bmatrix} = \begin{bmatrix} x_{N1_1} & 1 \\ x_{N2_1} & 1 \\ x_{N3_1} & 1 \\ x_{N4_1} & 1 \\ \vdots & \\ x_{Ni_j} & 1 \end{bmatrix} \begin{bmatrix} \beta_1 \\ \beta_0 \end{bmatrix} \tag{4.2}$$

Rearranging the equation in order to estimate the β, which can be written as:

$$\beta = (\mathbf{X}^T\mathbf{X})^{-1}\mathbf{X}^T\mathbf{y} \tag{4.3}$$

The Figure 4.3 shows the linear fit using least square represented by (—) which has a slope of 976.44 mN/V and an intercept of 5.33mN. (⊕) are the sampled mean of calibration

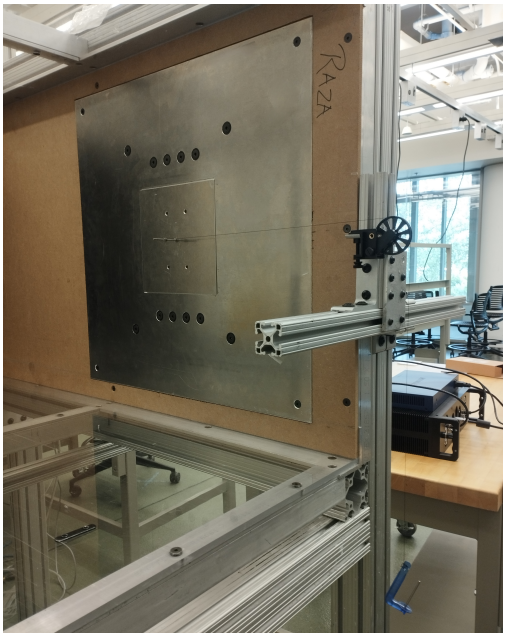


Figure 4.1: Floating element balance mounted on the wind tunnel wall for calibration process.

series with uncertainty in the mean $\pm\delta(V_{out}/V_{exc})$. The calibration data shows a scatter, especially at around $30mN$. The coefficient of determination R^2 is 0.99 , which shows that the linear fit is well and calibration data is satisfactory. The residual errors ϵ_{ER} in the linear fit for each observation can be approximated using the predicted values of the coefficients β and the experimental values of x.

$$\epsilon_{ER} = \mathbf{y} - \hat{\mathbf{y}} = \mathbf{y} - \mathbf{X}\hat{\beta} \tag{4.4}$$

The Equation 4.4 can be rewritten in matrix form as:

$$\epsilon_{ER} = \begin{bmatrix} \epsilon_{N1_1} \\ \epsilon_{N2_1} \\ \vdots \\ \epsilon_{Ni_j} \end{bmatrix} = \begin{bmatrix} y_{N1_1} - [\beta_1 x_{N1_1} + \beta_0] \\ y_{N2_1} - [\beta_1 x_{N2_1} + \beta_0] \\ \vdots \\ y_{Ni_j} - [\beta_1 x_{Ni_j} + \beta_0] \end{bmatrix} \tag{4.5}$$

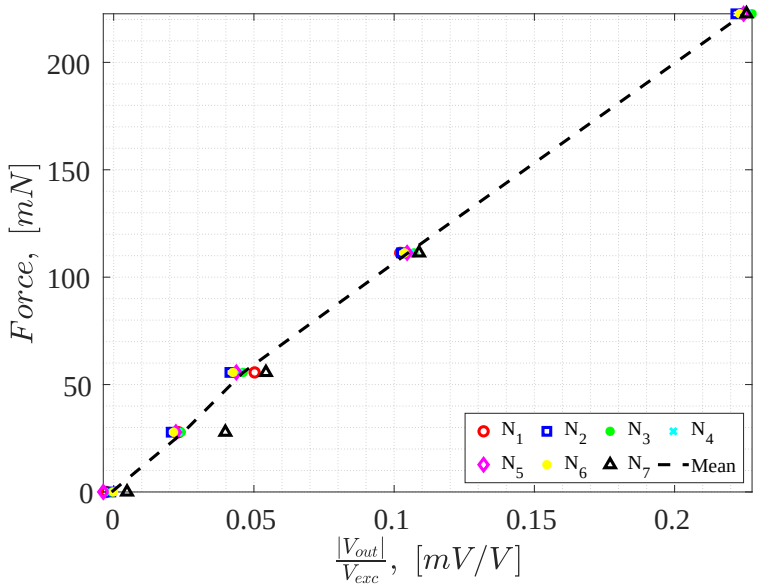


Figure 4.2: Calibration Data points, where N_i represents the calibration series, i represents number of series ($i = 1$ *to* 4 acquired before the wall shear measurements and $i = 5$ *to* 7 after the measurements). $(--)$ $\frac{|\overline{V_{out}}|}{V_{exc}}$: mean of the N_i series.

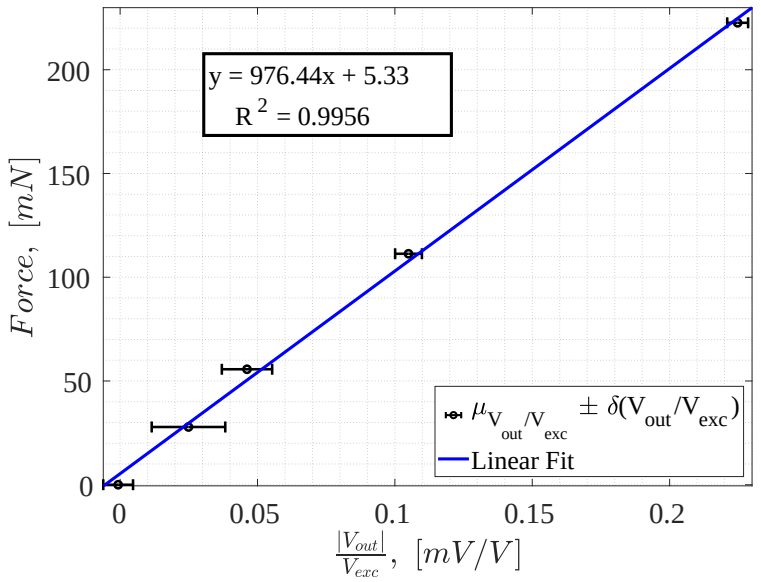


Figure 4.3: (—) : represents the linear fit $y = 976.44x + 5.33$ with $R^2 = 0.99$. $(\text{-}\!\!\text{o}\!\!\text{-})$ $\mu_{v_{out}/v_{exc}}$: mean of the N_i series and $\pm\delta(V_{out}/V_{exc})$ represents the measurement uncertainty in the mean

In equation Equation 4.5, $\epsilon_{N_{i_j}}$ represents residual error for a single point of the calibration series, where i is the number of series, and j is the corresponding output relative to the force. In the figure Figure 4.4, the residual errors of the calibration points are presented. (—) represents the linear fit . The residual errors of the post-measurement calibration points are higher compared to the pre-measurement calibration points. This increase is due to the drift and hysteresis in the strain gauge.

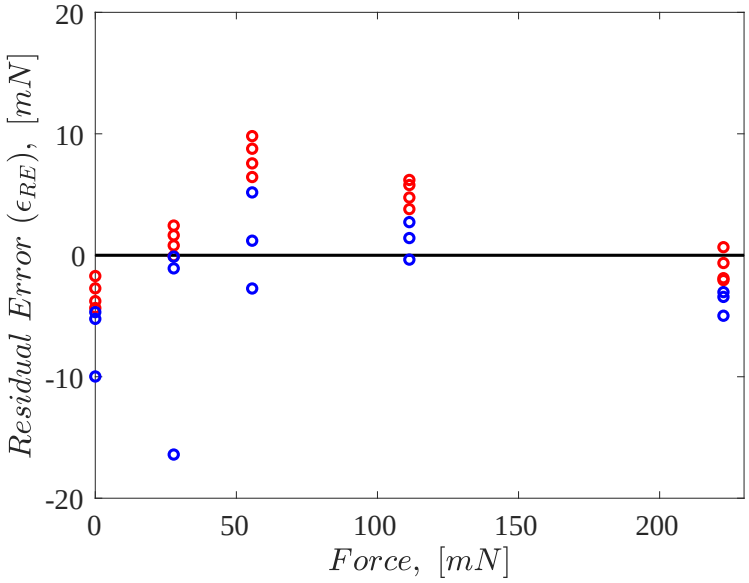


Figure 4.4: (—) : represents the linear fit $y = 976.44x + 5.33$, where y is the Force in units mN and x are the voltage output in mV/V. (o): taken before the wall shear measurements and (o): taken after the wall shear measurements

The Figure 4.5 presents the strain measurements from Figure 2.9, where the floating element balance was installed on an extruded aluminum frame. The black line denotes the mean from the long-term strain measurements compared with the calibration data acquired when the floating element balance was installed in situ Figure 4.2. The in situ calibration data and the long-term strain measurements are in agreement and within the estimated errors. This region of ≈ 0 *to* $200mN$ has inherent nonlinear effects as described in the section 2.3.

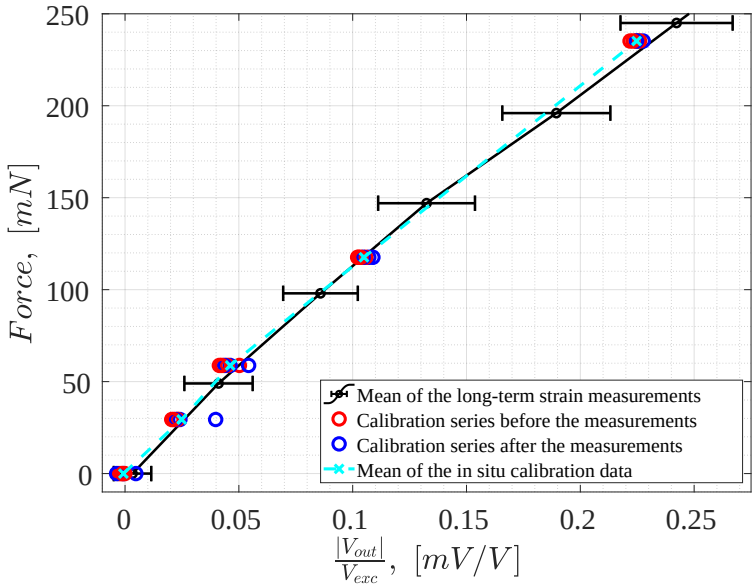


Figure 4.5: (—) : represents the strain measurements from Figure 2.9. (o): Calibration series before the wall shear measurements, (o): Calibration series after the wall shear measurements, and (-x -): Mean of the in situ calibration data.

4.2 Pitot Static Measurements

Pitot static probe measurements are presented in the Figure 4.6 courtesy of Chaware. The Pitot static probe measures static and stagnation pressure at a particular point. Using Bernoulli's principle, the dynamic pressure can be estimated. The traversing pitot static was used to create a wall-normal boundary layer velocity profile to study a surface-mounted obstacle. The pitot static tube was traversed in the wall-normal direction near the exit of the closed test section (not at the exact measurement point of the balance). The velocity profile can be used to estimate the coefficient of skin friction using the Clauser estimation (as discussed in section 1.3.1). The Figure 4.7 presents the velocity profile fitted to the Spalding profile. The coefficient of skin friction is estimated to be 4.0×10^{-3}.

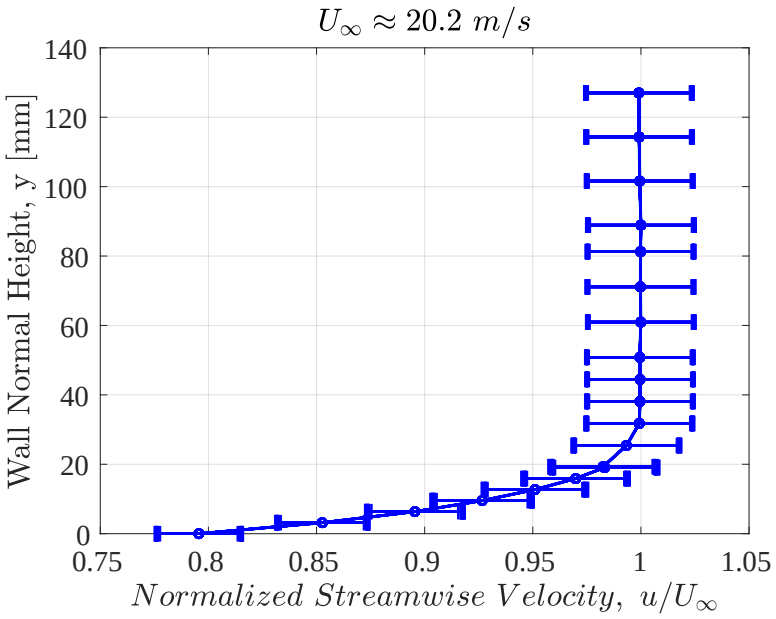


Figure 4.6: (▬) : represents the normalized streamwise velocity ($U_\infty \approx 20.2 m/s$) courtesy of Chaware. The error bars represents the uncertainty in the streamwise velocity.

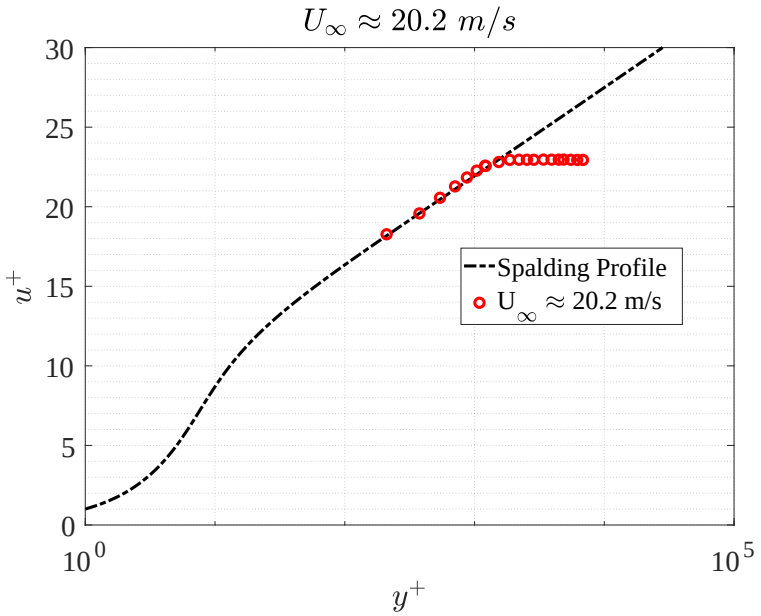


Figure 4.7: (▬ ▪ ▬): represents the Spalding profile. (o): represents the velocity profile fitted to the Spalding profile.

4.3 Steady Flow Measurements

After collecting the calibration data, the wind tunnel was powered up. The freestream velocity was kept constant for ≈ 1 *to* 2 minutes until the response of the signal was stable. The freestream velocity was gradually increased until reaching the maximum velocity of the wind tunnel ($\approx 26m/s$), followed by decreasing the freestream velocity until turning the wind tunnel off. This was followed by confirming that the signal response was stable before zeroing it. This process ensures that the first measurement point is recorded under the same conditions as the next measurement point[23]. The wind tunnel was powered on for wall shear measurement after the initial process, and the freestream velocity was increased slowly until reaching the desired freestream velocity.After the signal response stabilized at that particular freestream velocity, the data was sampled at $250kHz$ for 2 *minutes* to average the noise. The high sample rate highlights the high-frequency content recorded, which helps in the spectra study of the signal. For instance, the dominant energy peaks in the spectra will help understand the signal behavior. The data acquisition duration of 2 *minutes* was considered sufficient to establish stable response patterns in the voltage output. Alternatively, the acquisition duration can also be determined by utilizing the relationship of the boundary layer turnover time (as mentioned in [3, 23]). The signal average was used as an input to the linear fit equation (Figure 4.3) to determine the wall shear force. Two series of measurements were taken using the conditions described in the Table 4.1. Lastly, post-measurement calibration data was collected to study the drift in the response output.

The Figure 4.8 presents the wall shear force from the two measurements. The overall behavior of the wall shear stress is, as expected, increasing with the increase in freestream flow velocity. However, the estimated results of the force have contributions from both the wall shear and the pressure drag. The pressure drag is prominent due to the protrusion of the

Table 4.1: Steady flow conditions for wall shear measurements

Tunnel RPM	T_0 $(°C)$	P_0 $(mbar)$	ρ (kg/m^3)	μ $(Pa \cdot s)$	$P_\infty(in\ H_2O)$	$U_\infty(m/s)$
700	19.7	946.6	1.12	1.8×10^{-5}	0.54	15.30
800	19.6	946.1	1.12	1.8×10^{-5}	0.68	17.33
900	19.6	946.4	1.12	1.8×10^{-5}	0.88	19.72
1000	19.6	946.1	1.12	1.8×10^{-5}	1.05	21.45
1100	19.5	946.0	1.12	1.8×10^{-5}	1.28	23.62
1180	19.5	946.2	1.12	1.8×10^{-5}	1.47	25.53

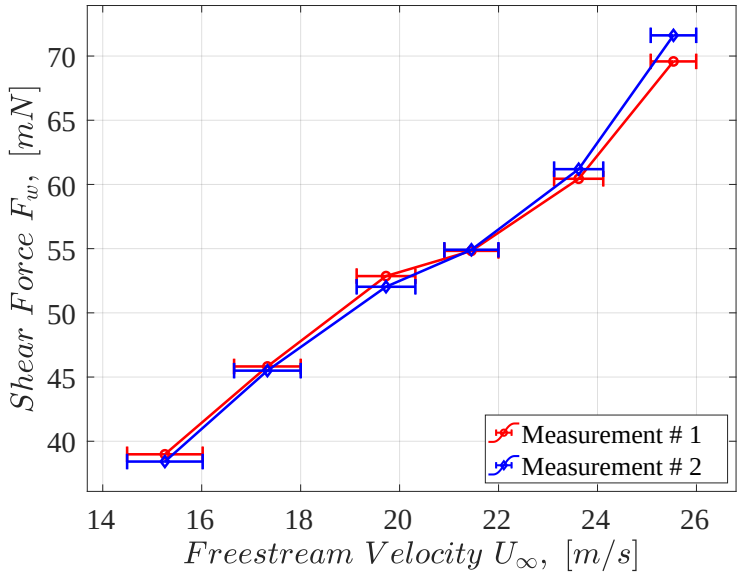


Figure 4.8: Results of wall shear estimated using the mean of the $F_w(t)$. (—) : Wall shear measurement series 1, and (—) : Wall shear measurement series 2. The error bars denotes the uncertainty in the freestream velocity

floating element (mentioned in section 2.4). The pressure distribution on the protruded lip of the element has overestimated the wall shear. Unfortunately, this effect makes it difficult to find the uncertainty in the wall shear stress. The Figure 4.9 shows the approximation of the skin friction coefficient with uncertainty in the dynamic pressure. The skin friction coefficients follow the expected trend, reducing with the higher velocities. The Spalding fit (as mentioned in section 4.2) provides a skin friction coefficient of $\approx\ 4\ \times\ 10^{-3}$ whereas the floating element balance estimates it $\approx\ 5.5\ \times\ 10^{-3}$ this overestimation due to the lip

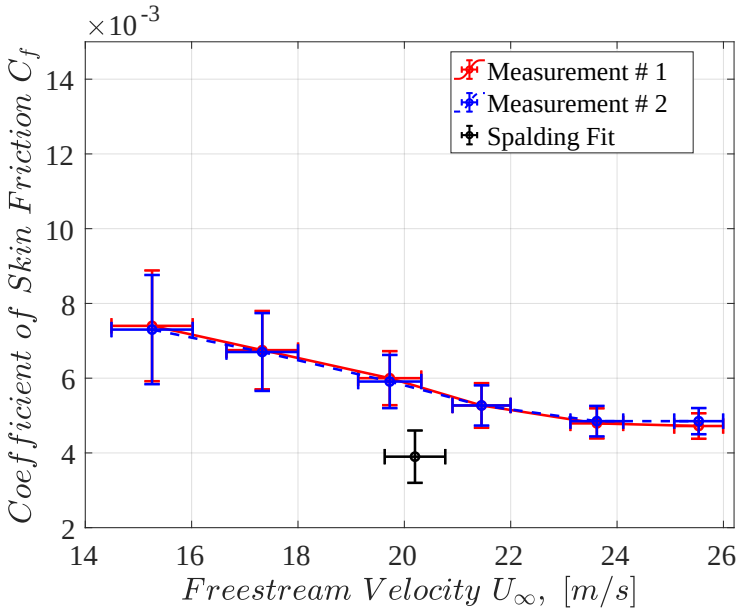


Figure 4.9: Coefficient of Skin Friction estimated using wall shear measurements and the dynamic pressure, error bars represents the uncertainty in the freestream dynamic pressure. o: represents the result of skin friction coefficient from Spalding profile (Figure 4.7).

forces. Note that the Spalding fit measurement is not at the same location or configuration as the floating element balance, but it was the only available data close to the measurement to provide a rough estimate.

It should be noted that the data below the lowest freestream velocity is not presented due to the vibrations from the wind tunnel fan, which was significant. However, the balance was sensitive enough to capture the wall shear at these higher freestream velocities. The trend shows that the balance will capture the wall shear at higher flow freestream velocity without overestimating it if the sensing element is fully flush-mounted. In addition, these measurements are taken from one transducer, so the uncertainty is relatively high in these measurements. The original plan was to use four sets of transducers both in upstream and downstream positions of the flexures (as mentioned in section 2.1). One possible way to improve the confidence in the measurements would be to use all of the flexures for transducers.

Alternatively, a semiconductor strain gauge will be even more beneficial in increasing the confidence of the measurements because of their high sensitivity and gauge factor.

4.4 Signal Post-processing

The signal of wall shear stress is shown in the Figure 4.10 from the $U_\infty \approx 15.30 m/s$. The signal shows high-frequency noise due to the vibration from the wind tunnel fan. The blue represents the raw data with a mean of $\mu_{F_w} = 0.0344 mV/V$ and a standard deviation of $\sigma_{F_w} = 0.0176 mV/V$. In comparison, the red represents the filtered signal by filtering the high-frequency content with a mean of $\mu_{F_w} = 0.0344 mV/V$ and a standard deviation of $\sigma_{F_w} = 0.0039 mV/V$. A low-pass filter was used to filter the signal. A cut-off frequency below the natural frequency of the balance can be selected at $\approx 2Hz$, which can filter out the noise from vibration due to the centrifugal blower. The estimation of the mean component of the wall shear stress can be further improved by increasing the sample duration.

The auto spectra in the Figure 4.11 are the voltage response of the wall shear measurements, estimated by using utilizing Welch's method averaging 114 records of FFT with 50% overlap. One feature of the measurements can be examined, such as the natural frequency of the balance, where the most dominant spectral peak exists $\approx 2.9Hz$, which is closer to the approximated f_n by using Euler-Bernouilli beam theory (described in section 2.2). It should be noted that floating element balance has an inherent low natural frequency response, and incorporating a means to push the natural frequency from this low-frequency region towards a much higher frequency region will provide much better spectral information.

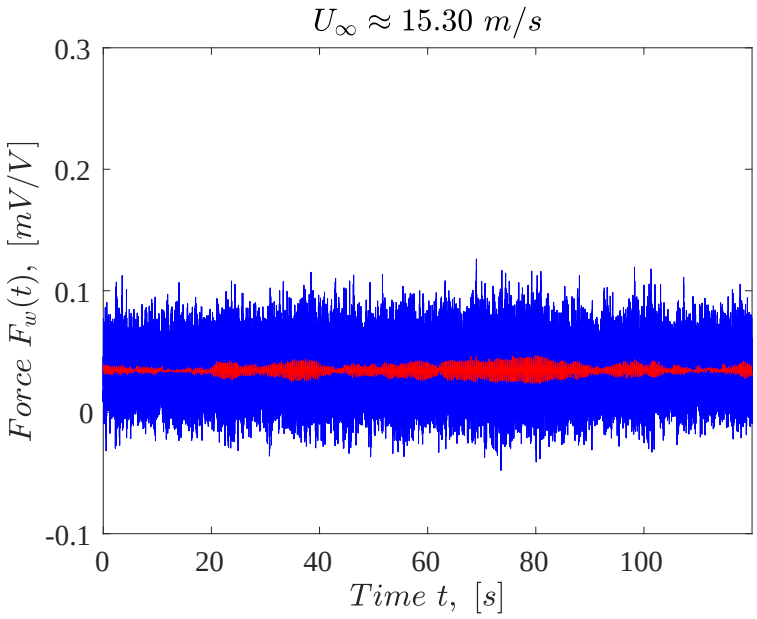


Figure 4.10: The time series of the $F_w(t)$ at $U_\infty \approx 15.30 m/s$ (▬) : represents the raw time series of the signal. (▬): represents the filtered signal at cutoff frequency of $\approx 2Hz$

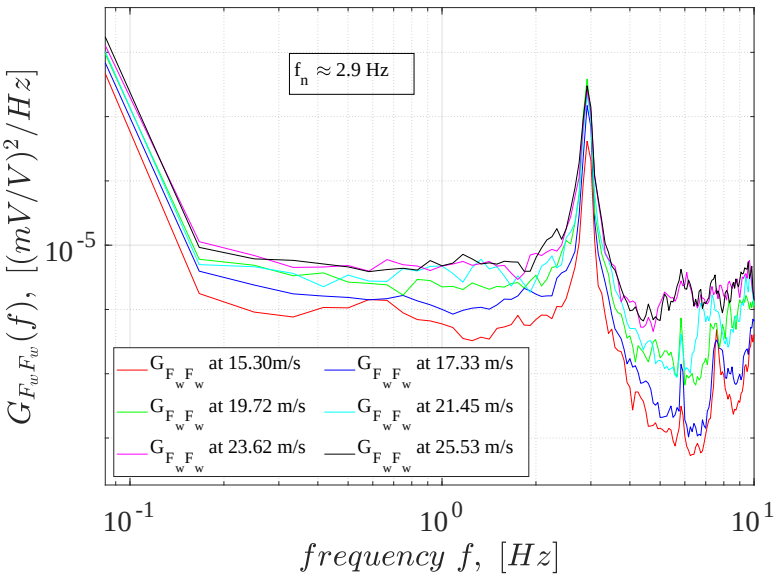


Figure 4.11: Auto spectra $G_{F_wF_w}(f)$ of the voltage response of the measurements highlights the dominant peak at $f_n \approx 2.9Hz$

Chapter 5

Conclusion

5.1 Summary

This study discusses the design and implementation of a floating element balance for a side wall of a wind tunnel for wall shear measurements. The importance of estimating wall shear stress lies in its inherent properties in fluid mechanics, mainly because it can characterize the flow. Another critical parameter is calculated by using wall shear stress, which is called the frictional velocity of the fluid, which is very challenging to estimate without experimentation. The design features a double parallel linkage mechanism constraining the motion in only a streamwise direction, which makes it insensitive to the wall-normal direction. An analysis of the strain is compared with the Euler-Bernoulli beam theory, and the experimental values show an agreement within 5% of the uncertainty. This study shows a calibration procedure that considers calibration data taken before and after the measurements using linear regression with a coefficient of determination of $R^2 = 0.99$. This linear curve equation is used to infer the wall shear from the steady flow measurements. The mean of the wall shear measurements is used as input for the curve equation. The approximated values of wall shear

stress show the expected behavior but are overestimated due to geometric inconsistencies in the design. The signal of wall shear stress is polluted by the vibration from the wind tunnel fan, which is filtered with a cutoff frequency of $< f_n$ the natural frequency of the floating element balance.

5.2 Recommendations

The proposed design requires more resolution in the sensing instrument. Perhaps a force transducer with a higher gauge factor could be used to improve the sensitivity of the transducer, capturing the slightest change in the signal. For instance, semiconductor strain gauges have a gauge factor in 100s while metal strain gauges have a gauge factor of ≈ 2. The measurement will always be prone to vibrations by the wind tunnel fan. Finding an efficient way to isolate the vibrations or study them will provide less noisy spectra, which can highlight fluctuating components of the wall shear. Alternatively, a tension-compression type force transducer can be utilized and installed in a way sensitive to only streamwise load, which will be more robust than a bending-type force transducer due to parasitic contributions from axial loading of the assembly. Furthermore, the aluminum panels can be fabricated with much more precision or can be $3D$ printed, ensuring the sensing element is fully flushed. The contributions from lip forces can be reduced by uniformly decreasing lip thickness with sharp ends. The mechanical seal between the fixed and floating surface in this study is a simple labyrinth seal, and adding a complex seal will reduce the disturbances from the flow. The proposed floating element design is a non-nulling device; a nulling floating element balance would improve the measurement because of its stable response. However, a nulling device is complex and requires an intricate counter-reactive mechanism that provides an equal and opposite force to the wall shear stress to keep the sensing element at the null position, which

will minimize the inherent errors associated with the floating element balance.

Bibliography

[1] JM Allen. Experimental study of error sources in skin-friction balance measurements. 1977.

[2] JM Allen. Improved sensing element for skin-friction balance measurements. *AIAA Journal*, 18(11):1342–1345, 1980.

[3] Woutijn J Baars, DT Squire, KM Talluru, MR Abbassi, Nicholas Hutchins, and Ivan Marusic. Wall-drag measurements of smooth-and rough-wall turbulent boundary layers using a floating element. *Experiments in Fluids*, 57:1–16, 2016.

[4] L Bairstow. Skin friction correction: A resume of investigations into boundary-layer theory, summarising knowledge on the subject. *Aircraft Engineering and Aerospace Technology*, 6(9):245–246, 1934.

[5] Thomas G Beckwith et al. *Mechanical measurements*. Pearson Education India, 2007.

[6] L Birk. *Fundamentals of Ship Hydrodynamics: Fluid Mechanics, Ship Resistance and Propulsion*. John Wiley & Sons, 2019.

[7] H Blasius. *The boundary layers in fluids with little friction*. Number 1256. National Advisory Committee for Aeronautics, 1950.

[8] KC Brown and PN Joubert. The measurement of skin friction in turbulent boundary layers with adverse pressure gradients. *Journal of Fluid Mechanics*, 35(4):737–757, 1969.

[9] Humza Butt, Shishir Damani, Surabhi Srivastava, Jarrod T Banks, Vidya Vishwanathan, William J Devenport, Todd Lowe, and Stewart A Glegg. Pressure gradient effects on low-wavenumber wall-pressure fluctuations in turbulent boundary layer flows. In *28th AIAA/CEAS Aeroacoustics 2022 Conference*, page 2803, 2022.

[10] Humza Butt, Shreyas S Chaware, Shishir Damani, Mate Szoke, Surabhi Srivastava, Todd Lowe, and William J Devenport. Characterization of the far-wake of a wall-mounted obstacle embedded in a turbulent boundary layer. In *30th AIAA/CEAS Aeroacoustics Conference (2024)*, page 3396, 2024.

[11] Yunus Cengel and John Cimbala. *Ebook: Fluid mechanics fundamentals and applications (si units)*. McGraw Hill, 2013.

[12] Shreyas Satish Chaware. *Study of Far Wake of a Surface-Mounted Obstacle Subjected to Turbulent Boundary Layer Flows*. PhD thesis, Virginia Tech, 2023.

[13] Kevin Chen. Analysis of oil film interferometry implementation in non-ideal conditions. 2010.

[14] Francis H Clauser. The turbulent boundary layer. *Advances in applied mechanics*, 4: 1–51, 1956.

[15] Donald Coles. The law of the wake in the turbulent boundary layer. *Journal of Fluid Mechanics*, 1(2):191–226, 1956.

[16] James W Dally, William Franklin Riley, and Kenneth G McConnell. *Instrumentation for engineering measurements*, volume 576. Wiley New York, 1993.

[17] Shishir Damani, Humza Butt, Jarrod T Banks, Surabhi Srivastava, N Agastya Balantrapu, Todd Lowe, and William J Devenport. Low-wavenumber wall pressure measurements in zero-pressure gradient boundary layer flow. In *AIAA SCITECH 2022 Forum*, page 1795, 2022.

[18] Lawrence J. De Chant. The venerable 1/7th power law turbulent velocity profile: a classical nonlinear boundary value problem solution and its relationship to stochastic processes. *Applied Mathematics and Computation*, 161(2):463–474, 2005. ISSN 0096-3003. doi: https://doi.org/10.1016/j.amc.2003.12.109. URL https://www.sciencedirect.com/science/article/pii/S0096300304000050.

[19] S. Dhawan. Direct measurements of skin friction. Technical Report Report 1121, NACA, 1953.

[20] Shivsai Ajit Dixit and ON Ramesh. Determination of skin friction in strong pressure-gradient equilibrium and near-equilibrium turbulent boundary layers. *Experiments in fluids*, 47(6):1045–1058, 2009.

[21] David M Driver. Application of oil-film interferometry skin-friction measurement to large wind tunnels. *Experiments in fluids*, 34:717–725, 2003.

[22] Julie E Duetsch-Patel, Vidya Vishwanathan, Jared B Minionis, Eric Totten, Aldo Gargiulo, Daniel J Fritsch, Máté Szoke, Aurelien Borgoltz, Christopher J Roy, Kevin T Lowe, et al. Aerodynamic design and assessment of modular test section walls for cfd validation in hybrid anechoic wind tunnels. In *AIAA Scitech 2020 Forum*, page 2214, 2020.

[23] M. Aguiar Ferreira, E. Rodriguez-Lopez, and B. Ganapathisubramani. An alternative floating element design for skin - friction measurement of turbulent wall flows. *Experiments in Fluids*, 2018. doi: https://doi.org/10.1007/s00348-018-2612-2.

[24] Michael C. Fischer and Robert L. Ash. A general review of concepts for reducing skin friction, including recommendations for future studies. Technical Memorandum NASA-TM-X-2894, NASA, Langley Research Center, Hampton VA 23665, USA, March 1974. URL https://ntrs.nasa.gov/citations/19740009864.

[25] D Frei and H Thomann. Direct measurements of skin friction in a turbulent boundary layer with a strong adverse pressure gradient. *Journal of Fluid Mechanics*, 101(1):79–95, 1980.

[26] Danny Fritsch, Vidya Vishwanathan, Julie Duetsch-Patel, Aldo Gargiulo, Kevin T Lowe, and William J Devenport. The pressure signature of high reynolds number smooth wall turbulent boundary layers in pressure gradient family. In *AIAA Aviation 2020 Forum*, page 3066, 2020.

[27] W. Froude. Experiments on the surface friction experienced by a plane moving through water. In *42nd British Association Report*, pages 118–124, 1872.

[28] Stewart Glegg and William Devenport. *Aeroacoustics of low Mach number flows: fundamentals, analysis, and measurement*. Academic Press, 2017.

[29] Joseph H Haritonidis. The measurement of wall shear stress. In *Advances in fluid mechanics measurements*, pages 229–261. Springer, 1989.

[30] F Hirt, U Zurfluh, and H Thomann. Skin friction balances for large pressure gradients. *Experiments in fluids*, 4(5):296–300, 1986.

[31] Sighard F Hoerner. Fluid-dynamic drag. theoretical, experimental and statistical information. *Copyright by: SF Hoerner Fluid Dynamics, Vancouver, Printed in the USA, Card Number 64-19666*, 1965.

[32] Karl Hoffmann et al. An introduction to measurements using strain gages. Technical report, Hottinger Baldwin Messtechnik Darmstadt, 1989.

[33] Nicholas Hutchins and Ivan Marusic. Large-scale influences in near-wall turbulence. *Philosophical Transactions of the Royal Society A: Mathematical, Physical and Engineering Sciences*, 365(1852):647–664, 2007.

[34] Nick Hutchins and Kwing-So Choi. Accurate measurements of local skin friction coefficient using hot-wire anemometry. *Progress in Aerospace Sciences*, 38(4-5):421–446, 2002.

[35] Hidetoshi Iijima, Takahiro Uchiyama, and Hiroyuki Kato. Temperature correction for oil film interferometry with infrared camera in skin friction measurements. *Journal of Visualization*, 24:657–664, 2021.

[36] Javier Jiménez. Turbulent flows over rough walls. *Annu. Rev. Fluid Mech.*, 36(1): 173–196, 2004.

[37] Günther Kempf. Neue ergebnisse der widerstandsforschung. *Werft Reederei u. Hafen*, 1929.

[38] SJ Kline and SK Robinson. Turbulent boundary layer structure: Progress, status, and challenges. In *Structure of Turbulence and Drag Reduction: IUTAM Symposium Zurich, Switzerland July 25–28, 1989*, pages 3–22. Springer, 1990.

[39] Fue-Sang Lien and Eugene Yee. Numerical modelling of the turbulent flow developing within and over a 3-d building array, part i: a high-resolution reynolds-averaged navier—stokes approach. *Boundary-Layer Meteorology*, 112:427–466, 2004.

[40] P Moin, T-H Shih, D Driver, and NN Mansour. Direct numerical simulation of a three-

dimensional turbulent boundary layer. *Physics of Fluids A: Fluid Dynamics*, 2(10): 1846–1853, 1990.

[41] Anthony F. Molland, Stephen R. Turnock, and Dominic A. Hudson. *Ship Resistance and Propulsion: Practical Estimation of Ship Propulsive Power*. Cambridge University Press, 2 edition, 2017.

[42] Alan S Morris and Reza Langari. *Measurement and instrumentation: theory and application*. Academic Press, 2011.

[43] Jonathan W Naughton and Mark Sheplak. Modern developments in shear-stress measurement. *Progress in Aerospace Sciences*, 38(6-7):515–570, 2002.

[44] W. Nitsche, C. Haberland, and R. Thunker. Comparative investigation on drag measuring techniques in experimental aerodynamics. In *Proceedings of the 14th ICAS Congress (ICAS-84-2.4.2)*, 1984.

[45] Francis B O'Donnell. *A study of the effect of floating-element misalignment on skin-friction-balance accuracy*. Defense Research Laboratory, the University of Texas, 1964.

[46] FJ Pierce and BB Zimmerman. Wall shear stress inference from two and three-dimensional turbulent boundary layer velocity profiles. *Journal of Fluids Engineering*, 1973.

[47] L. Prandtl. Über flüssigkeitsbewegung bei sehr kleiner reibung. In *Verhandlungen des 3. Internationalen Mathematiker-Kongresses, Heidelberg*, pages 484–491, 1904. Auch: Gesammelte Abhandlungen, 2, 484-491.

[48] E. Rathakrishnan. *Instrumentation, Measurements, and Experiments in Fluids*. CRC Press, 2nd edition, 2017. URL https://doi.org/10.1201/9781315365619.

[49] D Ronneberger and CD Ahrens. Wall shear stress caused by small amplitude perturbations of turbulent boundary-layer flow: an experimental investigation. *Journal of Fluid Mechanics*, 83(3):433–464, 1977.

[50] Hermann Schlichting and Klaus Gersten. *Boundary-layer theory*. springer, 2016.

[51] Fritz Schultz-Grunow. *New frictional resistance law for smooth plates*. Number 986. National Advisory Commitee for Aeronautics, 1941.

[52] Dudley B Spalding et al. A single formula for the law of the wall. *Journal of Applied mechanics*, 28(3):455–458, 1961.

[53] Stavros Tavoularis and Jovan Nedić. *Measurement in fluid mechanics*. Cambridge University Press, 2024.

[54] HM Tsai and DC Leslie. Large eddy simulation of a developing turbulent boundary layer at a low reynolds number. *International journal for numerical methods in fluids*, 10(5):519–555, 1990.

[55] Nguyen Van Le. The von karman integral method as applied to a turbulent boundary layer. *Journal of the Aeronautical Sciences*, 19(9):647–648, 1952.

[56] R. Vinuesa, R. Örlü, S. Discetti, and A. Ianiro. Measurement of wall-shear stress. In *Experimental Aerodynamics*, pages 393–428. CRC Press, 1st edition, 2017. doi: 10.1201/9781315371733-16. URL https://doi.org/10.1201/9781315371733-16.

[57] Vidya Vishwanathan. The resolution and structure of high reynolds number turbulent boundary layers over rough and smooth walls in pressure gradient. *Virginia Tech*, 2023.

[58] Vidya Vishwanathan, Danny Fritsch, Todd K Lowe, and William J Devenport. Analysis of coherent structures over a smooth wall turbulent boundary layer in pressure gradient

using spectral proper orthogonal decomposition. In *AIAA Aviation 2021 Forum*, page 2893, 2021.

[59] Vidya Vishwanathan, Daniel J Fritsch, K Todd Lowe, and William J Devenport. History effects and wall-similarity of non-equilibrium turbulent boundary layers in varying pressure gradient over rough and smooth surfaces. *International Journal of Heat and Fluid Flow*, 102:109145, 2023.

[60] Th Von Karman. Turbulence and skin friction. *Journal of the Aeronautical Sciences*, 1 (1):1–20, 1934.

[61] Xiong Wang, Nantian Wang, Xiaobin Xu, Tao Zhu, and Yang Gao. Fabrication and hypersonic wind tunnel validation of a mems skin friction sensor based on visual alignment technology. *Sensors*, 19(17):3803, 2019.

[62] S.P. Wilkinson, J.B. Anders, B.S. Lazos, and D.M. Bushnell. Turbulent drag reduction research at nasa langley: progress and plans. *International Journal of Heat and Fluid Flow*, 9(3):266–277, 1988. ISSN 0142-727X. doi: https://doi.org/10.1016/0142-727X(88)90037-9. URL https://www.sciencedirect.com/science/article/pii/0142727X88900379.

[63] K.G. Winter. An outline of the techniques available for the measurement of skin friction in turbulent boundary layers. *Progress in Aerospace Sciences*, 18:1–57, 1979. ISSN 0376-0421. doi: https://doi.org/10.1016/0376-0421(77)90002-1. URL https://www.sciencedirect.com/science/article/pii/0376042177900021.

[64] KG Winter. An outline of the techniques available for the measurement of skin friction in turbulent boundary layers. *Progress in aerospace sciences*, 18:1–57, 1979.

[65] Greg Zilliac, Thomas Pulliam, Melissa Rivers, Jordan Zerr, Maureen Delgado, Nettie

Halcomb, and Henry Lee. A comparison of the measured and computed skin friction distribution on the common research model. In *49th AIAA aerospace sciences meeting including the new horizons forum and aerospace exposition*, page 1129, 2011.